Charles University

Faculty of Science

Study programme: Inorganic Chemistry

FACULTY OF SCIENCE
Charles University

Mgr. Barbora Hyklová

Layered Transition Metal Hydroxides: Delamination and Properties
Vrstevnaté hydroxidy přechodných kovů, jejich delaminace a vlastnosti

Doctoral thesis

Supervisor: Ing. Kamil Lang CSc., DSc.

Supervisor-Consultant: RNDr. Jan Demel PhD.

Prague, 2017

Prohlášení

Prohlašuji, že jsem pracovala samostatně a že jsem uvedla veškeré zdroje, ze kterých jsem čerpala. Dále prohlašuji, že tato práce ani její podstatná část nebyla předložena k získání jiného nebo stejného akademického titulu.

V Řeži, 23. Listopadu 2017

Acknowledgement

I am deeply grateful to both my supervisors Ing. Kamil Lang CSc., DSc. and RNDr. Jan Demel PhD. for their help and support during my doctoral research. Also, I would like to thank all the colleagues from the laboratory.

I am also grateful to my co-workers for measurement of various instrumental techniques: RNDr. Petr Bezdička PhD. for XRD diffraction, Ing. Eva Večerníková for FTIR spectra and DTA, RNDr. Jan Rohovec PhD. for ICP-MS and Ing. Josef Pleštil CSc. for SAXS.

I also thank to my family and friends for support during my study.

Table of content

List of abbreviations

AAS	Atomic absorption spectroscopy
AFM	Atomic force microscopy
CTABr	Hexadecylammonium bromide
DS	Dodecyl sulphate anion
DTA	Differential thermal analysis
EDS	Energy-dispersive X-ray spectroscopy
FTIR	Fourier transformation infrared spectroscopy
HMT	Hexamethylene tetraammine
HOPG	Highly oriented pyrolytic graphite
ICP-MS	Inductively coupled plasma mass spectrometry
Lac	Lactate anion
LCoH	Layered cobalt hydroxide
LDH	Layered double hydroxide
LHS	Layered hydroxide salt
LNiH	Layered nickel hydroxide
LNiCoH	Mixed layered nickel-cobalt hydroxide
MMO	Mixed metal oxide
MOF	Metal-organic framework
NMR	Nuclear magnetic resonance
SAXS	Small angle X-ray scattering
SDS	Sodium dodecylsulfate
SEM	Scanning electron microscopy
TEM	Transmission electron microscopy
TGA	Thermogravimetric analysis
TMD	Transition metal dichalcogenides
UV-Vis	Absorption spectroscopy
XRD	X-ray diffraction

Abstract

Layered transition-metal hydroxides have attracted increasing attention as promising active electrode materials for electrochemical energy storage and conversion device due to facile preparation and modification, good tunability, high capacitance capability, fast reversible redox reactions, and cost effectiveness. Many reported hierarchical architectures based on nickel and cobalt hydroxides are composed of bulky nanoplatelet-like aggregates; however, the nanomorphology and behavior of the nanosheet ultrathin films is much less known.

The dissertation thesis reports characterization and electrochemical performance of nickel, nickel-cobalt, and cobalt hydroxide nanosheets, synthesized by an economical and environmentally friendly method. For this purpose, lactate and nitrate layered hydroxides were prepared by two synthetic procedures (i.e., alkaline precipitation and anion exchange reaction), which led to the products with different properties and compositions.

The hydroxide nanosheets were prepared by delamination of corresponding layered hydroxide lactates or nitrates in water. Resulted transparent colloids were stable for months. Dispersions form transparent gels at higher concentrations (>30 mg mL^{-1}). In all cases, the delamination was well reproducible and practically quantitative. The morphology of the hydroxide nanosheets was investigated by small angle X-ray scattering method (SAXS), AFM, and TEM evidencing the presence of the single hydroxide nanosheets of approximately 1 nm thickness.

The nanosheets in the resulting colloids were restacked to form ultrathin electrodes for the study of electrochemical behaviour not affected by the bulk effects. The voltammetric curves of prepared electrodes showed different behaviour than that of corresponding thicker films. The study indicates that Co-doping in mixed nickel-cobalt hydroxide nanosheets improved the performance of the nanosheets by decreasing the time of their electrochemical activation, which for the pure nickel hydroxide nanosheets requires much more potential sweeps. Thanks to the nanometric thickness, the ultrathin electrodes showed very fast electrochemical response in the comparison with the conventional bulky materials. The nanosheets prepared by the present method show promise for use in nanocomposite materials for energy storage applications.

Abstrakt

Vrstevnaté hydroxidy přechodných kovů jsou známé jako elektrodové materiály použitelné pro konstrukci baterií a superkapacitorů. Mezi jejich hlavní přednosti patří snadná příprava a následné modifikace, vysoká elektrická kapacita, rychlé elektrochemické děje a nízká cena. Většina publikovaných elektrochemických studií o vrstevnatých hydroxidech přechodných kovů se zabývá pouze objemovými materiály, naopak elektrochemické vlastnosti příslušných nanomateriálů jsou mnohem méně prozkoumané.

Tato dizertační práce se zabývá charakterizací a elektrochemickými vlastnostmi nanodesiček vrstevnatých hydroxidů niklu a kobaltu připravených levnou a k životnímu prostředí šetrnou metodou. Byly připraveny vrstevnaté hydroxidy interkalované laktátovými a dusičnanovými anionty za použití dvou rozdílných postupů (přímým srážením a iontovou výměnou), které vedly k produktům s odlišnými vlastnostmi a složením.

Příslušné nanodestičky byly připraveny delaminací výše zmíněných hydroxidů ve vodě za vzniku transparentních a stabilních koloidních roztoků. Ve všech případech byla delaminace dobře reprodukovatelná a kvantitativní. Při vyšších koncentracích (>30 mg mL^{-1}) měly připravené disperze podobu transparentních gelů. Velikost a tvar nanodesiček byl určen pomocí rozptylu rentgenového záření koloidem při malých úhlech (SAXS), a mikroskopickými technikami AFM a TEM. Spojením těchto metod byl prokázán vznik separovaných hydroxidových nanodesiček s tloušťkou kolem 1 nm.

Připravené koloidní roztoky byly použity pro přípravu elektrod pro následná voltametrická měření. Tyto elektrody tvořené nandodestičkami vrstevnatých hydroxidů niklu a kobaltu nejsou díky své nanometrické tloušťce zatížené pomalou difuzí iontů do elektrody jako v případě objemových materiálů a jsou tak schopny velmi rychlé elektrochemické odezvy. Dále bylo zjištěno, že tenké nanodestičkové filmy obsahující kobalt potřebují k elektrochemické aktivaci mnohem méně cyklů než filmy tvořené pouze čistým hydroxidem nikelnatým, což činí elektrochemickou aktivaci kobaltových elektrod mnohem rychlejší. Z výsledků vyplývá, že nanodestičky vrstevnatých hydroxidů kobaltu a niklu jsou slibnými nanokompozitními materiály pro konstrukci baterií nebo superkapacitorů.

1. Introduction

Layered materials are utilized by humankind for a long period of the history due to their unique properties arising from their structural anisotropy. Clay minerals have been used for making ceramics and dyes thanks to their plasticity, swelling ability and intercalation property. Graphite, on the other hand, is widely known as a mineral for scribing. The first commercial use dates to 16th century, when graphite was used for the first time for pencil manufacturing.[1] Although the layered materials were utilized for centuries, the two-dimensional (2D) structure was understood in the first half of 20th century, after the discovery of X-ray diffraction analysis. The structure consists of layers with atoms strongly bonded to each other by covalent bonds, whereas, bonding interactions between the neighbouring layers are weak leading to the strong anisotropy of chemical and physical properties.[2,3]

1.1 Layered materials

The archetypal example of layered material is graphite consisting of hexagonal graphene sheets bound together by weak π-π interactions.[1,4,5] Another example are clay minerals, a group of natural or synthetic layered silicates, which contain tetrahedrally coordinated silicon and octahedrally coordinated metals like aluminium or magnesium forming negatively charged layers with balancing cations in the interlayer gallery.[1,6] The layered structure can be found in many other materials with different chemical compositions such as transition metal chalcogenides,[7] metal halides,[8] metal oxides and related charged materials (e.g., titanates, niobates and layered transition metal hydroxides).[9,10,11,12,13] Zeolites, which are known 3D porous materials, can be transformed into a pseudo-layered structures by delamination or pillaring in order to combine advantages of materials with layered and porous structure.[14] The lamellar structure leads to the variety of typical chemical and physical properties like mechanical, thermal and electric conductivity anisotropy or absorption, intercalation and exfoliation ability.

1.1.1 Intercalation

Layered, chain and porous materials can reversibly incorporate various guest species like atoms, ions and molecules.[15] Guest incorporation takes place without significant changes of the host lattice structure, but it can fundamentally influence the properties of resulting materials. There are two basic modes of host-guest incorporations: insertion and intercalation. In the case of insertion, the host lattices are 3D nonlamellar materials, typically framework structures with pores like zeolites or metal-organic frameworks (MOFs), and the guest molecules do not change the structure significantly.[16,17] Intercalation is reversible uptake into structures consisting of layers or chains bonded by weak chemical interactions or electrostatic forces.[15,18] Whereas guest insertion into framework materials is strongly limited by a pore size, layered and chain hosts have far smaller demands on a guest size because of the expandable nature of their structure. The key limit lays in weakening of electrostatic interactions in the case of very large intercalated species, leading to a low ordering or even to disintegration of the structure.[15]

The host lattices can be neutral (graphite, boron nitride, transition metal chalcogenides and halides), negative (clay minerals, oxides and phosphonates) or positive (layered hydroxides) and therefore the guest species have to bear complementary charge.[15] In the last few decades, the most often studied neutral intercalation materials are graphite intercalation compounds containing neutral guests such as alkali metals, layered metal halides or various oxides, acids or salts.[1,19] In all cases, the structure consists of graphene sheets separated by intercalated species and the physical properties like conductivity, magnetic or mechanical properties strongly differ from pure graphite. One of the most important industrial applications are Li-ion batteries where the electrochemical reaction is based on reversible intercalation of Li^+ into a graphite anode.[20,21]

In the case of charged hosts, the intercalated ions have charge-balancing functions and therefore they are the integral part of the material structure.[22] The typical examples of negative host lattices are clay minerals, which consist of silicate layers with balancing cations in the interlayer. The nature of the cation can range from simple alkali metals ions to bulky organic molecules.[6,23] The group of clay minerals known as smectites can absorb water which lead to swelling of the structure. This ability is crucial for clay plasticity and utilization in ceramic manufacturing or as absorbents.[1] Most important members of the intercalation compounds with positive host lattice are layered hydroxides. The reason of the positive charge is the deficit of hydroxide groups or the presence of trivalent cations in the hydroxide layers. The positive charge is compensated by interlayer anions ranging from simple inorganic anions to complex organic molecules. Similarly to clay minerals, layered hydroxides contain water molecules in the interlayer and some of them are able to swell in suitable solvents. Anion exchange reactions and delamination are also common for layered hydroxides.[12,13]

1.1.2 Nanosheets

Tremendous effort has been devoted to studying nanoparticles with strong shape anisotropy, among those, 2D nanoparticles or nanosheets have a prominent place[2,24] The most often studied is graphene possessing excellent in-plane electric conductivity and mechanical strength.[25,26] Many other nanosheets have been prepared in the last two decades, for example transition metal oxide nanosheets mostly containing the MO_6 units, where M is typically Ti^{4+}, Nb^{5+} or $Mn^{3+,4+}$. Oxide nanosheets are usually negatively charged containing balancing metal cations in the interlayer space, and they are studied for their magnetic or photocatalytic properties and for solar cell constructions.[27,28,29] Other materials like transition metal dichalcogenides (TMD) or boron nitride also exist in the form of nanosheets which have wide range of applications in electronic, optoelectronic or composite material fabrication.[30,31] Hydroxide and clay mineral nanosheets are often used for the preparation of nanocomposites and hybrid materials.[32,33]

An ideal nanosheet should consist of one monolayer which limits the thickness from few angstroms to approximately one nanometre. The monolayer can have monoatomic thickness, as in the case of graphene, or it can consist of more atoms as is the case in clay minerals. In some cases, the preparation method does not lead to the ideal monolayer nanosheet, but to the thicker nanoparticles composed of more stacked layers. These nanoparticles can be also called nanosheets, but the number of the stacked layers should be small (typically 2-10) with a thickness not exceeding several nanometres.[2,34] It should be noted that the resulting properties can depend on the number of layers, as demonstrated by varying properties of single-layer and multi-layer graphene.[35] The nanosheet lateral dimension can range from tens of nanometres to several hundreds of micrometres. The shape anisotropy and nanometric dimension are responsible for specific physical and chemical properties which differ from the corresponding bulk material. One of the most interesting features of nanosheets is their self-assembling ability.[33] Due to their platelet shape, nanosheets are able to restack into the bulk materials or arrange regularly on a surface to new hybrid materials, composites or thin films.[36,37] A flocculation is typical example of restacking. It is based on the addition of a suitable guest compound into a nanosheet solution. The guest interacts with the layers leading to aggregation and the formation of a new intercalation compound. Self-assembly of nanosheets on a surface forming oriented film is other example of restacking. The simplest way for self-assembly is drop casting where the colloid is slowly evaporated on various surfaces.[38] More sophisticated methods can provide not only highly oriented films, but also films with controllable thickness and composition.[39,40] The most often utilized methods are spin coating and dip coating. In the last twenty years, several new deposition methods including ink-jet printing or layer-by-layer method (LBL) have been developed.[41] Ink-Jet printing is based on the same principle as common ink printers. Tiny droplets of colloid are precisely deposited by a printhead onto a substrate. The LBL method is based on sequential spontaneous electrostatic deposition of layers bearing electrostatic charge. The method enables to tailor the thickness and composition for specific electronic, optical or catalytic applications.[42,43]

There are two main strategies for the nanosheet preparation: the bottom-up approach based on the direct synthesis of nanosheet from molecules and the top-down approach based on the separation of respective nanosheets from the bulk material (Figure 1)[33] The former approach often utilizes surfactants, which form micelles serving as microreactors or templates. Because of the space limitation in microemulsion, produced nanosheets have a narrow size distribution.[44] The nanosheet dimensions can be also controlled by reaction conditions including surfactant concentration, temperature or solvent. For example, uniform nanosheets of Ca/Al layered double hydroxide can be prepared in the presence of sodium dodecyl sulphate. The nanosheet diameter ranges from 20 to 100 nm depending on a dodecyl sulphate/water ratio.[45] The nanosheets can also be grown by chemical or physical deposition techniques on atomically flat surfaces.[46]

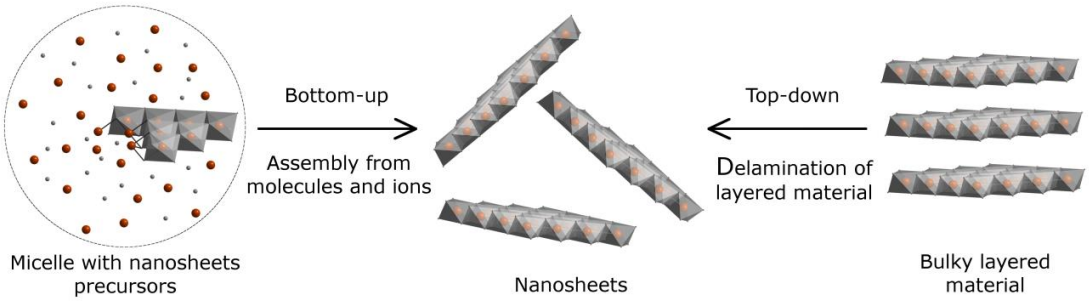

Figure 1. Schematic illustration of the two main strategies for nanosheet synthesis: bottom-up (left) and top-down (right).

The top-down approach is more frequent and is commonly called delamination or exfoliation.[2] The weakening of the bonding forces holding the layered material together can be performed either by mechanical or chemical means. The typical example of the mechanical delamination is the isolation of graphene sheets from graphite by micromechanical cleavage using a scotch tape.[25,47]

The chemical delamination is a promising alternative to the mechanical cleavage. It is based on the separation of layered material using a suitable solvent forming colloidal solution of nanosheets.[2] In this case, the energetic situation in the solvent–host–guest system is crucial. The overall thermodynamic stability of colloid solution can be quantified by zeta potential of the dispersed particles, which is defined as the potential difference between the distant point in bulk solution and the slipping plane of the interfacial double layer surrounding the particle. More practically, it could be explained as the repulsion among particles dispersed in colloid solutions. The systems with low zeta potentials tend to aggregate, whereas in the case of high zeta potentials, the repulsion interactions are strong leading to stable colloid solutions and successful delamination. Because zeta potential is influenced not only by solvent (polarity and surface tension), but also by the nature of nanosheets (overall charge, polarity, solvation properties) and guest species (polarity, solubility, solvation properties), the delamination can be enhanced by intercalation of suitable guest, chemical modification of the layer surface or change of the lattice charge density. The most known example is the oxidation of graphite and subsequent ultrasound exfoliation of prepared graphene oxide in water.[48,49]

Intercalation of suitable guests affects the interlayer bonding forces whose weakening leads to successful delamination. Moreover, the guest molecules are part of the solvation layer surrounding the nanosheet and thus influence the zeta potential. This method can be applied to neutral layered materials, but it is more often used for delamination of charged host lattices like layered oxides, hydroxides and clay minerals which contain exchangeable balancing ions. For example, bulky guest ions such as *t*-butyl ammonium or dodecyl sulphate are often utilized for layered materials which are intended to be delaminated. Delamination can be also enhanced by elevated temperature, microwave irradiation or sonication.[2] The latter method is based on ultrasound cavitation in solution and subsequent formation of microbubbles mechanically separating bound layers.[50] Generally, the process of delamination is very complex and the understanding and predictions of this phenomenon are still more empirical than theoretical.

1.2 Layered hydroxides

Hydroxides of less electropositive metals and transition metals often possess the layered structure composed of metal cations connected by OH groups. The simplest layered hydroxides contain closely packed neutral layers consisting of metal cations and hydroxide groups with no interlayer molecules resulting in a tight basal spacing and small capability to delaminate or intercalate. Magnesium hydroxide (mineral brucite, $Mg(OH)_2$) is a typical example. Its structure is composed of octahedrally coordinated magnesium cations connected by edges forming an infinite layer with the thickness of 0.477 nm (Figure 2). The layers are held together by weak chemical interactions like dispersion and hydrogen bondings and the layers are tightly packed with an interlayer distance of 4.8 Å. The structures of most of layered double hydroxides (LDH) and layered hydroxide salts (LHS) are closely related to that of brucite.[51]

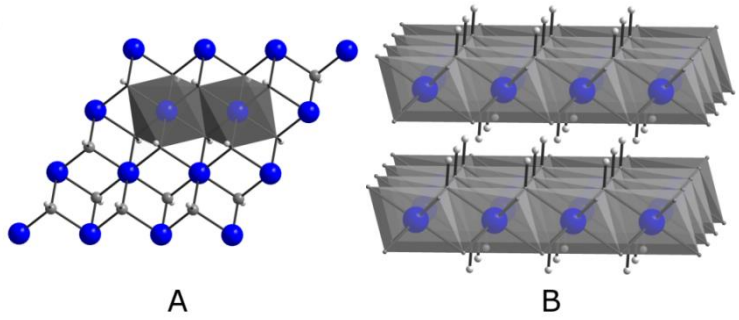

Figure 2. Brucite structure: Top view of the octahedrally coordinated magnesium atoms in a single sheet (A); Side view of two stacked brucite layers (B). Mg atoms are blue, O atoms are dark grey and H atoms are white.

LDH and LHS contain positively charged layers due to the deficit of hydroxide groups or the presence of metal cations in higher oxidation state.[12,13,52] These hydroxides always contain water and charge balancing anions in the interlayer space which results in a basal spacing varying from 6 Å to 35 Å, depending on the balancing anion size and arrangement. The presence of anions and solvent molecules causes also weakening of the interlayer bonding interactions and expansion of the whole structure which facilitates anion exchange reactions, intercalation and delamination.[15] The balancing anions can be also tailored organic functional molecules. This strategy leads to the new organic-inorganic hybrid materials that combine synergistic effects of functional molecules with a variable inorganic matrix.[53]

The delamination of layered hydroxides was for a long time limited to polar organic solvents like formamide or butanol due to the high charge density of the hydroxide layers.[27,33] The high price and toxicity of these solvents led to efforts to use water as a delamination solvent. For this purpose, the hydrophilic and polar anions appear to be the best choice. The first successful delamination of layered hydroxides in water was achieved by intercalation of lactate anions into Mg/Al LDH, since then several LDHs were delaminated using hydrophilic anions like acetates or sulfonates. [54,55,56]

1.2.1 Layered double hydroxides (LDH)

LDHs are the most often studied group of layered hydroxides. The positive layer charge is caused by the presence of trivalent cations in the brucite-like layers. The general formula of LDHs is $[M^{2+}_{1-x}M^{3+}_{x}(OH)_2]^{x+}[A^{n-}]_{x/n}\cdot yH_2O$, where M^{2+} and M^{3+} are metal cations and A^{n-} is the intercalated anion (Table 1).[12,51]The content of trivalent cations typically lies in the range of $0.2 < x < 0.33$. Both cations must have the same coordination number and the geometry of the structural site giving the limiting size difference of cations, commonly approximately $2 \cdot 10^{-2}$ nm. Some LDHs slightly differ from general structural aspects, e.g., ternary or quaternary "LDHs", or LDHs containing monovalent and trivalent cations ($[LiAl_2(OH)_6][A^{n-}]_{1/n}\cdot yH_2O$). LDHs with the uncommon M^{2+}/M^{3+} ratio (up to $x = 0.5$) or the cation size ratio were also prepared. LDHs in nature are represented by mineral hydrotalcite with the general formula $Mg_6Al_2(OH)_{16}CO_3\cdot 4H_2O$, where carbonates are balancing anions.

Table 1. Typical composition of LDHs ($[M^{2+}_{1-x}M^{3+}_{x}(OH)_2]^{x+}[A^{n-}]x_{/n}\cdot yH_2O$.)

M^{2+}	Ca^{2+}, Mg^{2+}, Mn^{2+}, Fe^{2+}, Co^{2+}, Ni^{2+}, Cu^{2+}, Zn^{2+}, etc.
M^{3+}	Al^{3+}, Co^{3+}, Cr^{3+}, Fe^{3+}, V^{3+}, etc.
A^{n-}	Inorganic anions (Cl^-, Br^-, CO_3^{2-}, NO_3^-, SO_4^{2-}, etc.), Organic anions (carboxylates, sulfonates etc.), Complex organic molecules and bio molecules (aromatics, porphyrins, polymers, amino acids, DNA, etc.)

1.2.3 Layered hydroxide salts (LHS):

Layered hydroxide salts contain metal cations only in one oxidation state and the layer charge originates from the deficit of hydroxide groups.[13] The most common LSHs contain only one type of metal ion, but others containing two different divalent metal cations (layered double salts) are also known. There are two structural types of brucite-based LHS (Figure 3.).[57]

The general formula of one structural type is $[M^{2+}_2(OH)_3]A^{n-}_{(1/n)} \cdot yH_2O$ and it is typical for Ni^{2+} (α-polymorph) and Cu^{2+}. These LHSs contain only octahedrally coordinated divalent cations and the layers are isostructural with brucite (Figure 3A). The second type has a triple deck structure consisting of the brucite layers where one quarter of the octahedral ions is replaced by tetrahedral ions located below and above the octahedral plane (Figure 3B). The general formula of this structural type is $[M_5(OH)_8]A^{n-}_{(2/n)} \cdot yH_2O$ and it is typical of Zn^{2+} or Co^{2+} (α-polymorph). The described structures represent the ideal composition of LHSs. Real structures can contain many defects influencing for example the number of tetrahedral ions or layer charge.[58] Rare earth metals also form LHSs, however, due to their high coordination number the structure of the layers is characterized by orthorhombic or monoclinic space groups. The typical formula is $[M^{3+}_2(OH)_5]A^{n-}_{(1/n)} \cdot yH_2O$, where M is trivalent rare earth metal ion (Figure 3C).[59]

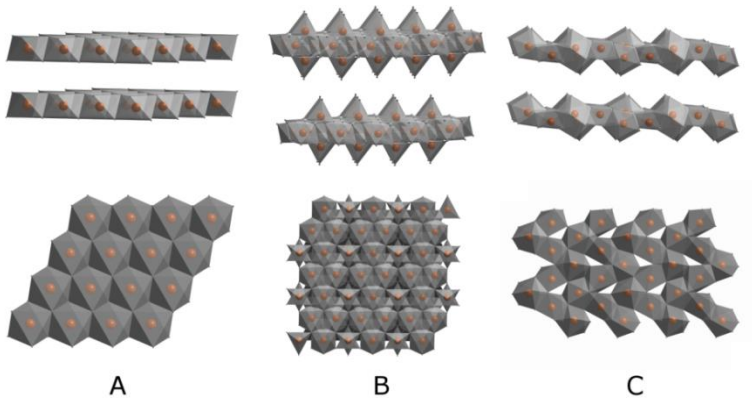

Figure 3. Schematic structure of LHS: (A) $[M^{2+}_2(OH)_3]A^{n-}_{(1/n)} \cdot yH_2O$, (B) $[M_5(OH)_8]A^{n-}_{(2/n)} \cdot yH_2O$, (C) Rare earth layered hydroxide salt. The interlayer anions and water molecules are not displayed for better clarity.

1.3 Synthesis of layered hydroxides

Although the synthesis of layered hydroxides is based on simple approaches, the reaction conditions strongly influence the phase purity, structure, composition and morphology.[51] For example, the pH value or temperature during the synthesis can influence the LDH M^{2+}/M^{3+} ratio as well as the particle size distribution. The used synthetic methods are briefly discussed below.

1.3.1 Precipitation

Most of LDHs are prepared by slow and controlled mixing of M^{2+}/M^{3+} solution with sodium hydroxide solution at constant pH. There are several principles which should be abided for the successful preparation of a pure LDH phase.[12,51] Intercalated anions must be present in an excess during the precipitation in order to obtain the pure phase. The value of pH is crucial in order to ensure the homogeneous distribution of both cations within the hydroxide layers. Typical pH values used for alkaline precipitation of LDHs range from 6 to 10, depending on precipitated cations. The pH value should not change during the precipitation in order to avoid the contamination by $M(OH)_2/M(OH)_3$ impurities or the formation of LDH phases with undesired M^{2+}/M^{3+} ratios. It is also necessary to avoid the presence of CO_2, which has large affinity to the basic LDH phase and could be spontaneously intercalated between the hydroxide layers in the carbonate form.

The preparation of LHSs is based on similar principles developed for LDHs, but it is generally less difficult because LHSs can be precipitated from acidic or neutral solutions without the need of pH control. LHSs also consist of less basic transition metals with lower affinity towards carbon dioxide, so LHSs can be precipitated in air atmosphere. However, certain conditions have to be maintained; for example, the amount of alkaline hydroxide used for the precipitation has to be cautiously controlled in order to avoid the formation of undesired oxides and hydroxides.[13] A low crystallinity of LHSs is a common complication accompanying the preparation. The crystal size and crystallizing can be improved by fine tuning of the reaction conditions, such as the ratio of the reactants or aging in the mother liquor at elevated temperatures.

1.3.2 Hydrothermal precipitation

The method is based on the slow generation of ammonia by hydrothermal decomposition of nitrogen containing compound such as urea or hexamethylenetetraamine (HMT). [12,13,51] The main advantage is the higher crystallinity of prepared layered hydroxides in comparison with simple alkaline precipitation. The synthesis is a one-pot reaction where metal salts, anion and ammonia releasing agent are present in the same solution. After heating to 70-100°C, depending on the ammonia precursor, ammonia is slowly released thus increasing the pH and, as a result, hydroxide precipitates from the solution. Urea decomposes to ammonium cyanate and, in the second step, to ammonium carbonate. The pH value of the ammonium carbonate hydrolysis is about 9 and it is suitable for the precipitation of many LDHs and LHSs. The main disadvantage is possible intercalation of released carbonate anions, which contaminate the designed phase. HMT is more suitable because it decomposes to formaldehyde and ammonia without the formation of carbonate anions.

1.3.3 Ion exchange methods

Ion exchange requires pre-synthesized parent layered hydroxide intercalated with exchangeable anion.[12,13,51] This method is especially useful when precipitation methods are not applicable; for example, when precursors or final products are not stable during co-precipitation, direct precipitation produces by-products, or when anions preferably react with metal ions to form salts or complexes. In a typical procedure, parent layered hydroxide is dispersed, stirred or shaken in the excess of the anion solution. Elevated temperature and long reaction times up to several days are often required for successful anion exchange. The exchange of anions is often incomplete.

The main factors influencing the anion-exchange reactions are attractive electrostatic interactions between the host lattice and exchanging anions and the free energy connected with changes of hydratation.[51] Anions intercalated in parent layered hydroxides strongly influence the attractive electrostatic forces holding them inside the interlayer, therefore they must be carefully chosen. Generally, small and multiply charged anions are more difficult to exchange. The order for monovalent small inorganic anion is $OH^- > F^- > Cl^- > Br^- > NO_3^- > I^-$ and therefore nitrates are often the anions of a choice for parent layered hydroxides. Some organic anions also proved to be very successful for exchange reactions; for example, dodecyl sulphate anions (DS) are widely used. The process can be enhanced by the addition of cationic surfactant such as hexadecylammoniumbromide (CTABr) which helps to remove DS from the interlayer space by ion-pair formation.[60] The chemical composition of the hydroxide layers also inflicts the exchange ability because it influences the charge density of the host lattice and the affinity toward specific anions. Solvent polarity also plays an important role as it influences the solubility of leaving anions. For example, anion exchange of polar inorganic anions is favoured in aqueous solutions, whereas organic solvents are more suitable for the exchange of organic anions.

1.3.4 Other methods

There are several methods which are applicable only to a specific group of layered hydroxides.[12,13,51] For example, some LDHs (Zn/Cr or Zn/Mn) and LHSs of Zn^{2+} and Co^{2+} can be prepared by the hydrolysis of solid metal oxides in the solution of metal salts or acids; in this case metal salt anions are intercalated between the layers. LDHs can be also prepared by rehydration using the structural memory effect. This method is based on calcination of parent LDH to the corresponding oxide followed by rehydration with aqueous solution of desired anions, leading to the restoration of the LDH structure. The rehydration must be performed under inert atmosphere in order to avoid carbonate contaminations. The method is suitable for intercalation of large anions and its main advantage is avoiding competitive anion intercalation from metal salts.

Layered hydroxides containing Ni, Co or Fe cations can be also prepared by electrochemical synthesis. [61] Co^{2+}/Co^{3+} and Mg^{2+}/Fe^{3+} LDHs can be synthesized from corresponding LHSs by controlled oxidation of metal cations.[62]

1.4 Characterization techniques

1.4.1 Powder X-Ray diffraction analysis

The most important instrumental method for the qualitative phase analysis is powder X-ray diffraction (XRD).[51] A typical X-ray diffraction pattern of layered hydroxides (Figure 4) contains basal diffractions on the basal hydroxide layers corresponding to the interlayer distance. The position of the first basal line lies in the range between 35 – 6 Å (2.5 and 14 °2θ, Cu Kα), depending on the nature, size and arrangement of intercalated anions, and on amount of interlayer water molecules. In the case of well-crystalline samples, the large number of diffraction lines corresponds to the multiples of the basal spacing. The XRD patterns of layered hydroxides containing basal diffractions of several interlayer distances can reveal several hydroxide phases with different interlayer anions or interstratification, i.e., the regular alternation of the layers with a different interlayer arrangement.

Diffraction lines corresponding to the facets, which are not parallel to the hydroxide layers, are localized at higher diffraction angles. These nonbasal diffractions are independent on intercalated anions and often form broad composite maxima due to stacking faults and turbostraticity. The positions of these basal diffraction bands are similar for all layered hydroxides with a brucite-like structure (approximately 33, 58 and 68 °2θ, Cu Kα). (Figure 4).

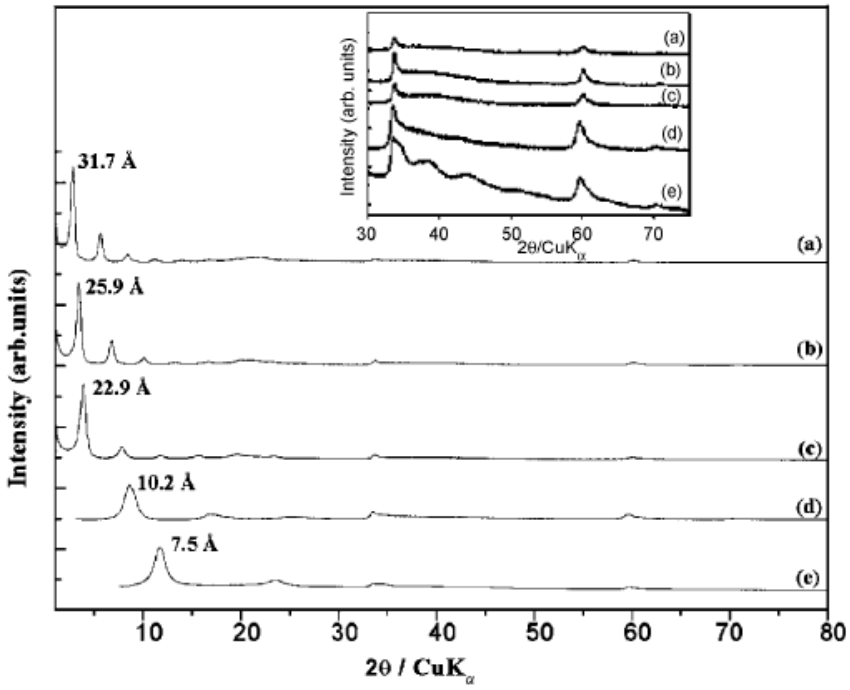

Figure 4. The brucite-type layered nickel hydroxides with different intercalated anions: LNiH-$C_nH_{2n+1}SO_3$ a) n=18, b) n=14, c) n=10, d) LHS-Ni-Ac, e) LHS-Ni-NO_3. Basal maxima in the area from 0 to 15 °2Θ depend on intercalated anion, whereas nonbasal diffractions related with hydroxide layers in the area from 30 to 80 °2Θ are in the same position for all displayed hydroxides. Reproduced from {M. Taibi, S. Ammar, N. Jouini, F. Fiévet, P. Molinié, M. Drillon, *J. Mater. Chem.*, **2002**, *12*, 3238-3244}[63] with permission of The Royal Society of Chemistry.

Layered hydroxides have due to their 2D nature platelet morphology causing the self-organisation and preference orientation of sample grains. The preference orientation is evidenced by changes in the peak intensity in comparison with randomly oriented materials. In an XRD reflection mode, the preference orientation increases the intensity of diffraction lines corresponding to the facets parallel with the sample surface (i.e., basal diffractions), whereas the diffraction intensity of nonbasal diffractions is considerably suppressed. The intensity changes in the XRD transmission mode are opposite, thus, the comparison of the XRD patterns collected in both reflection and transmission modes can serve as an evidence of the preferential orientation and documents successful restacking of nanosheets to form an oriented film.

1.4.2 Spectroscopic methods

Although XRD analysis is an effective tool for qualitative analysis, it has limitations in providing information about the chemical composition or contamination with anions of a similar size. Moreover, XRD analysis cannot directly detect amorphous phases. In order to overcome this problem, diffraction techniques must be combined with other analytical methods from which the spectroscopy is the most frequent. These methods can provide information about the chemical composition, arrangement of interlayer anions and solvent molecules, the coordination sphere and valency of the metal cations. It could also identify of amorphous impurities or contaminants.

Infrared spectroscopy (FTIR)

Infrared spectroscopy is a strong characterisation method for analysing the chemical composition and arrangement of intercalated molecules or molecules. Typically, layered hydroxide shows characteristic vibration bands of surface and interlayer water molecules approximately at 3500 cm^{-1} (stretching O-H vibrations band broadened by hydrogen bonding) and between 1600 and 1650 cm^{-1} (δ H-O-H vibration band) (Figure 5). Hydroxide groups attached to the inorganic layers have vibrations between 750 and 550 cm^{-1} represented by the broad composite vibration band.[63] Other bands correspond to the characteristic vibrations of interlayer anions, which can be used not only as the evidence of anion composition and presence in the interlayer space, but they can also provide the information about their symmetry, coordination and arrangement. The typical example is distinguishing of free and attached intercalated anions based on their different symmetry observed for simple inorganic anions such as nitrates or carbonates.[57] The determination of the carboxylate coordination mode is another example. The energy difference between symmetrical and asymmetrical carbonyl vibrations can indicate the type of the bond coordination – monodentate, bidentate or ionic.[64]

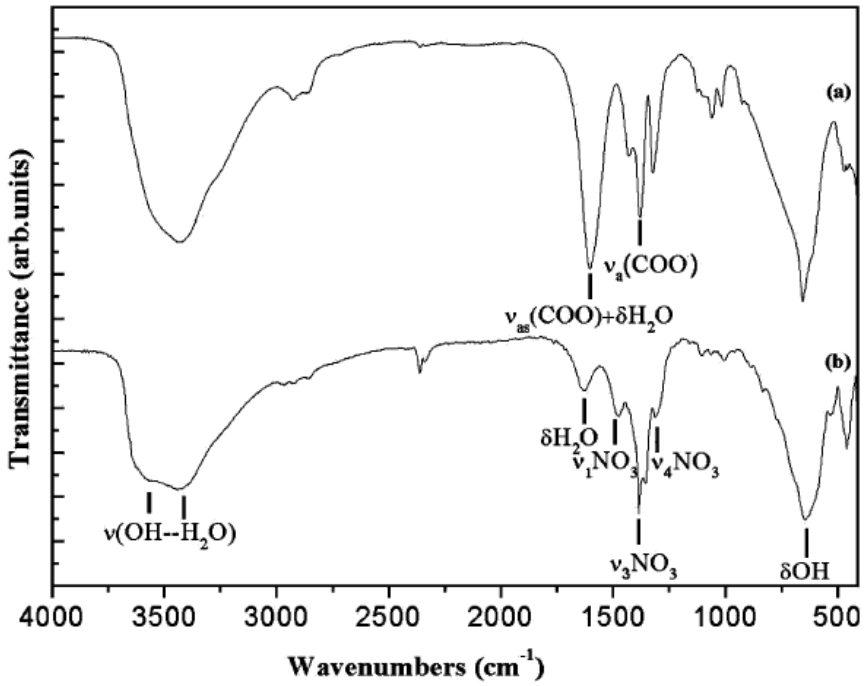

Figure 5. FTIR spectra of layered nickel hydroxide intercalated by acetate (a) and nitrate (b) with typical layered hydroxide vibration bands as well as the bands corresponding to the interlayer anions. Reproduced from {M. Taibi, S. Ammar, N. Jouini, F. Fiévet, P. Molinié, M. Drillon, *J. Mater. Chem.*, 2002, *12*, 3238-3244}[63] with permission of The Royal Society of Chemistry.

UV-Vis spectroscopy

UV-vis spectroscopy can be used for studying the hydroxide layer or intercalated anions, although it does not provide detailed structural information due to the broad and complex composite absorption bands which frequently overlap. However, many transition metals have electronic d-d transitions in the visible and ultraviolet region which can be useful for the analysing the hydroxide layer structure and composition. The absorption bands of certain metal ions are strongly dependent on their oxidation state, therefore transition metal ion pairs such as Fe^{2+}/Fe^{3+} or Co^{2+}/Co^{3+} are distinguishable by UV-Vis spectroscopy. The d-d transitions can be also influenced by the coordination sphere of metal ions. Divalent cobalt ion is the typical example: octahedral coordination is pink, tetrahedral is blue or green, and planar coordination is characterized by red or pink colour (Figure 6.).[65]

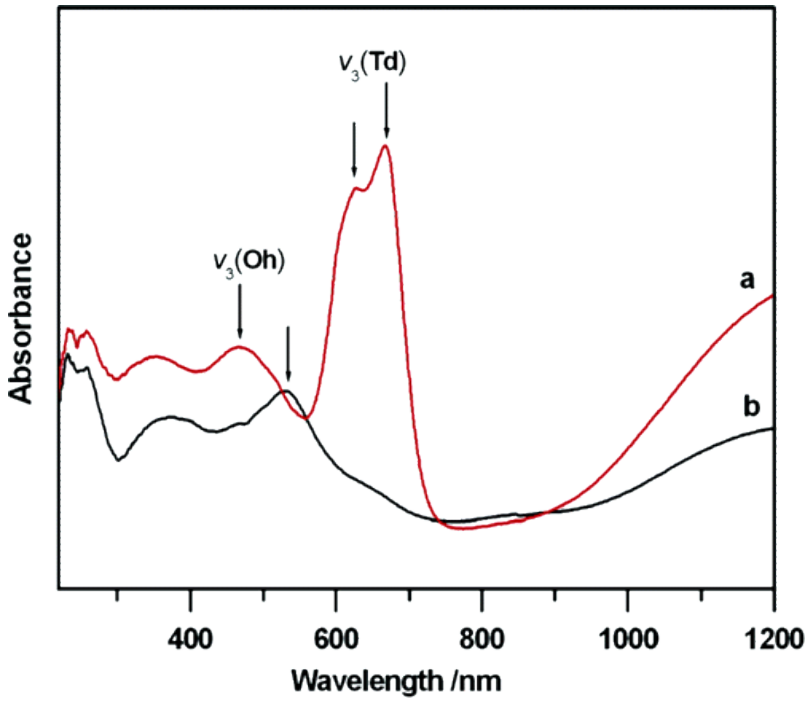

Figure 6. α $Co(OH)_2$ (a) and β $Co(OH)_2$ (b) differ by structure. Tetrahedral (v_3(Td)) and octahedral (v_3(Oh)) coordination of Co^{2+} are clearly distinguishable by UV-vis spectroscopy. Reprinted with permission from (R. Ma, Z. Liu, K. Takada, K. Fukuda, Y. Ebina, Y. Bando, T. Sasaki, *Inorg. Chem*. **2006**, *45*, 3964-3969).[65] Copyright (2006) American Chemical Society.

UV-vis spectroscopy is used for studying coloured interlayer anions such as aromatics, porphyrin-like molecules, transition metal complexes or dyes. The UV-Vis spectra of free and intercalated anions could differ due to electronic interactions with the host lattice and neighbouring anions or can be influenced by the anion arrangement. For example, monomeric porphyrin and porphyrin aggregates can be distinguished by UV-Vis spectroscopy due to their different band positions and intensities[66]. UV-Vis spectroscopy can be also employed in quantitative analysis, because the band absorbance is proportional to the amount of absorbing molecules. This approach is advantageous in LBL film preparations, where the increasing anion absorption band should be proportional with the number of layers.[67]

Other spectroscopic methods

Fluorescence spectroscopy is commonly used for investigation of luminescent layered hydroxides either containing intercalated photoactive dyes such as porphyrins or rare earth ions in the hydroxide layers.[66,68] Fluorescence properties, i.e., quantum yield, excitation and emission wavelengths, lifetimes of excited states, can be influenced, similarly to UV-Vis spectra, by interlayer anion arrangement or by interaction between anions and host lattices.

NMR spectroscopy of layered hydroxides is limited to the solid state measurements. Conventional ^{13}C NMR spectroscopy could be useful for layered hydroxide intercalated by organic anions[69] and ^{35}Cl NMR is especially useful for chloride intercalated layered hydroxides because these anions cannot be studied by infrared spectroscopy.[51] In recent years, ^{27}Al NMR spectroscopy was utilized for M^{2+}/Al^{3+} LDH studies.[70]

Mossbauer spectroscopy was used for the characterization of iron-containing layered hydroxides like M^{2+}/Fe^{3+} LDHs or LDHs intercalated by $[Fe(CN)_6]^{3-/4-}$ complexes.[51] This method can provide information about the oxidation state or M^{2+}/Fe^{3+} ratio.[71]

1.4.3 Differential thermal analysis and thermogravimetry (DTA/TGA)

Thermal behaviour is commonly studied by the DTA/TGA method based on slow and controlled thermal degradation of the sample with the simultaneous measurement of a total mass. The combination with a mass spectrometer allows gas detection during the thermal decomposition. Typical layered hydroxide decomposes in several steps and the decomposition can be reversible as in case of LDH.[57,72] The first step around 100°C is connected with the release of surface and interlayer water. The mass decrease corresponding to this step can be used for estimation of the amount of water molecules. The second step is connected with the total degradation of the layered hydroxide structure. This step occurs at temperatures above 150 °C and it is accompanied by the release of water originating in the hydroxide groups. The third step corresponds to the interlayer anion degradation accompanied by significant mass decrease and evolution of corresponding gases such as carbon, sulphur or nitrogen oxides. Temperature of this degradation step depends on the nature of the anions and can be lower than 200 °C in the case of simple anions like simple carboxylates, or higher for bigger organic molecules. Certain interlayer anions decompose at high temperatures, for example, sulphate anions are decomposed above 600°C. The final products of layered hydroxide thermal degradation are mostly corresponding metal oxides whose subsequent thermal phase transformations can be also detectable by the DTA/TGA analysis.

1.4.4 Microscopic techniques

The structure and morphology of layered hydroxides can be studied by various microscopic techniques, among them electron microscopy represented by scanning and transmission electron microscopy (SEM, TEM) and atomic force microscopy (AFM) are the most frequent. Although these methods are crucial for morphological studies of layered hydroxides, the methods display only a small selected part of the sample and it is always questionable if the measured results are representative for the whole sample. SEM is commonly used for the crystal size and shape determination. TEM can provide further information on the nanometric scale about the lateral dimension, shape and arrangement of deposited materials, but thanks to the electron diffraction, it can also provide information about the crystallinity and crystallographic orientation of the respective particles. Moreover, the detection of the EDS signal provides basic elemental analysis. The main limitation of TEM connected with measuring of layered hydroxides lays in the sensitivity to a high energy electron beam causing the degradation of the measured sample. This can be overcome by cooling the sample, use of a suitable matrix or measurement at lower accelerating voltages or vacuum. AFM is complementary to the TEM, because it detects the vertical profile of the deposit with the subnanometer accuracy. AFM is often employed for the determination of the thickness of nanosheets. The lateral dimension derived from AFM is always disputable, because the measured images are convolutions of the shape of the sample and probe tip. Related scanning probe microscopy techniques can be also utilized for the investigation of electric and magnetic properties of a deposited material.

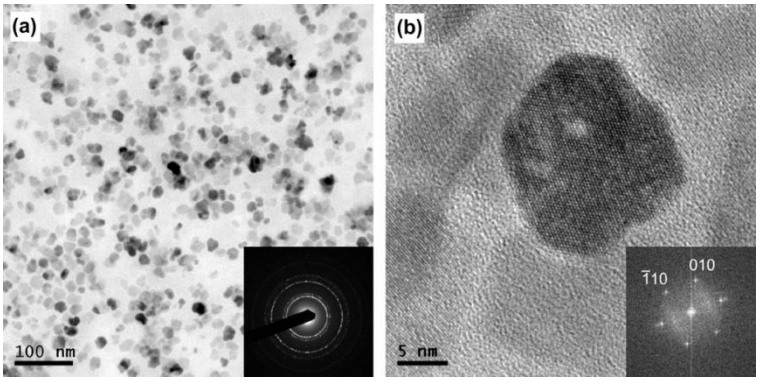

Figure 7. HRTEM images of ZnO nanoplatelets prepared from zinc hydroxide nanosheets in butanol.[73]

1.4.5 Small angle X-ray scattering (SAXS)

The method was developed for the morphological studies of solid particles in colloid solutions or polymer matrices. The method is based on the measurement of X-ray scattering on dispersed particles.[74] Although the interpretation of measured data is not straightforward, this method brings useful information about the particle dimension, shape and size distribution. Unlike the microscopy techniques, SAXS can provide information on the morphology of the particles *in* situ in colloid solution or polymer matrix avoiding the possible changes connected with a sample preparation and handling. Moreover, the gained information does not correspond only to a small volume of the sample, but to the whole volume and therefore the measured properties are representative for the bulk colloid. The information provided by SAXS can be successfully used for studying of hydroxide nanosheet colloids and can provide an evidence of successful delamination.

1.4.6 Elemental composition

The determination of elemental composition can provide information about the amount and ratio of metals in hydroxide layers. Although classical analytical methods including titrations can be strong tools, for example, for metal-cation valency determination, the most important methods for obtaining elemental composition are instrumental techniques. The analysis are mostly based on dissolution of layered hydroxides in suitable acid and determination of metals in resulting solutions by atomic absorption spectroscopy (AAS) or inductively coupled plasma mass spectrometry (ICP-MS). The classical elemental analysis, which commonly measures the amount of C, H and N and also other elements like O and S, can be utilized for the determination of interlayer anions and impurities.

1.5 Applications of layered hydroxides

The applications of layered hydroxides are mainly based on intercalation, ion exchange, composite fabrication and thermal degradation to corresponding oxides.[12,13] LDHs has the most notable industrial usage containing polymer additives, flame retardants, catalysis and absorbers.[75] Except of these examples, LDH and LHS were studied as prospective new materials for medicine applications or power cell constructions.

1.5.1 Polymer additives

One of the largest application fields is the fabrication of polymer composites containing LDHs. The addition of LDHs influences mechanical, thermic or optical properties.[76,77] The preparation is often based on intercalation of polymers between hydroxide layers and layered hydroxides are often present in the form of nanosheets.[33] LDHs are often used as PVC stabilizers preventing thermal degradation and dechloration, which is for pure PVC typical. The mechanism of the stabilization is based on the reaction of released HCl with the interlayer anions and hydroxide layers causing the degradation of the layered structure and the formation of metal chlorides.[78] Other application is based on utilization of LDH-based flame retardants. Simple layered hydroxides, e.g., $Mg(OH)_2$ and $Al(OH)_3$, are the most utilized flame retardants, because they are cheap and relatively nontoxic in comparison with commonly used halogen-based materials. Recently, Mg/Al LDHs were also used as a new generation of flame retardants due to their unique composition and layered structure with intercalated borates which are known for their flame-retardant properties.[79] The principle of a polymer flammability reduction lays in the absorption of heat during hydroxide thermal decomposition accompanied by water vapour release. Moreover, layered hydroxides could also serve as smoke absorbers, decreasing the probability of suffocation.[80] Other application consists in LDH-containing polymer horticultural foils, which are well-transparent for sun light, but less transparent for infrared radiation. These foils were used for greenhouse covering minimizing the thermal loses during the night, whereas the transparency for sun light necessary for photosynthesis was unchanged.[12]

1.5.2 Materials for catalysis

Layered hydroxides are an important class of materials for heterogeneous catalysis due to a large number of basic sites. The catalysts are based on LDHs or more frequently on their calcination products known as mixed metal oxides (MMO) which has well-defined composition and homogenous distribution of the active sites, thermal stability and large surface area. LDHs can be also used as matrices for catalytically active interlayer anions or as immobilizers for homogenous catalysts.[81,82,83]

LDH and MMO catalysts can be used in many base-catalysed organic reactions, involving the single and double carbon-carbon, carbon-nitrogen and carbon-oxygen bonds formation such as the Knoevenagel condensation, Michael addition, aldol condensation, epoxidation, arylation and many others.[82] The morphology of layered hydroxide catalysts also plays an important role, for example, the smaller particles possess higher surface areas and therefore show higher catalytic activity due to a larger number of accessible basic sites. Layered hydroxides can be supported on a suitable surface like mica or carbon nanofibers, which facilitate the mass transport.[81] The catalysis could be also realised by the presence of photoactive or electroactive transition metal cations in the structure. For example, the electrocatalytic activity can be promoted by the introduction of Ni, Co or Fe cations, which are capable catalysing redox reactions such as water and alcohol splitting.[84,85] Alternatively, LDH-containing cations of Zn, Ti, Nb and Cr can be utilized as semiconductor photocatalysts for organic pollutants degradation or for water decomposition splitting.[81]

Layered hydroxides can intercalate a large number of catalytically active molecules and, can be used as a support for homogeneous catalyst immobilizations.[82] There has been a large number of catalytic centres immobilized in the LDH matrixes: organometallic Pd and Rh catalysts, polyoxometalates, metal complexes and catalytically active biomolecules such as amino acids, proteins and enzymes. The intercalation could enhance the stability and recyclability of a catalyst. Moreover, the intercalation could influence the structural arrangement of the catalytic centres and thus enhance the catalyst activity as well as selectivity.[81] For example, layered hydroxides intercalated with planar aromatic photoactive molecules such as metalloporphyrins show better photocatalytic properties than free metalloporphyrins due to the suppressing of aggregation and catalyst deactivation.[66]

1.4.3 Metal-oxide precursors

Layered hydroxides can be used as precursors for various metal oxides, which are mostly prepared by calcination at temperatures above 300 °C or by solvothermal treatment.[13,51] Magnetic, optical or catalytic properties of prepared oxides are strongly dependent on the purity and microstructure of the active material and these properties are strongly influenced by a synthetic procedure.[12] There are many examples showing that oxides prepared by thermal decomposition of LDH have better magnetic or catalytic performance than oxides prepared by other techniques like vapour deposition or sol-gel methods. For example, iron containing mixed oxides with the spinel structure $M^{2+}M^{3+}{}_2O_4$ prepared by LDH calcination show much higher saturation magnetisation than spinels prepared by other techniques. Different example can be the preparation of ZnO nanosheets with the high amount of catalytically active {001} facets by solvothermal decomposition of delaminated layered zinc hydroxide salt in butanol at relatively low temperature of 60 °C.[86]

1.5.4 Materials for absorption and separation

The intercalation and anion exchange properties predetermine layered hydroxides for absorption or selective separation of anionic molecules. These applications are widely utilized in the case of clay minerals and zeolites, but in recent years layered hydroxides are often used as well. Their main advantage lays in the ability to absorb negatively charged species contrary to other absorbers. For example, LDHs were studied as absorbers for industrial wastes such as harmful nitrogen or sulphur oxides or different oxo-anions such as arsenates, chromates, phosphates.[87] The selective separation properties can be demonstrated by layered zinc or copper hydroxide salts showing high selectivity for isomers of naftoic acid. Zinc and nickel double hydroxide salts are selective for SeO_3^{2-} in solution containing also chlorides and nitrates anions.[13]

1.5.5 Materials for biological applications

The earliest applications of layered hydroxides in medicine were focused on antiacidic and antipeptic properties.[74] In recent years, a lot of effort has been devoted to the intercalation of bioactive molecules into LDH matrices. The most frequently used bio-anions are amino acids, nucleotides, DNA, vitamins and drugs. The prepared materials are studied mostly for gene and drug delivery, cosmetics or biosensing.[12,88,89] The main advantages of LDHs are not only the low toxicity and simple synthesis, but also their high anion exchange properties, high drug loading capacity and protection of intercalated drugs.[90] Several LDH biohybrids were tested *in-vivo* for medical applications. For example, LDH was utilized for the delivery of DNA vaccine, which enhances the anti-melanoma immune response.[91] Different examples are implants coated by ciprofloxacin antibiotic intercalated LDH, which were successfully used for the treatment of rabbits infected by chronic otitis media.[92] LDHs were also tested for cosmetic applications, which are aimed mostly to UV protection or release of drugs from inorganic matrices and subsequent penetration to the skin.[88] Thus, LDH materials interlaced with vitamins A, E and C show a higher skin penetration rate than pure vitamins.

1.5.6 Applications based on electrochemical properties

Layered hydroxides containing electrochemically active transition metal cations such as Fe, Ni, Co or Mn can be used for electrochemical applications including the construction of power cells, capacitors or sensors.[93,94,95,96,97] Their functionality is based on reversible oxidation of hydroxide to oxide-hydroxide accompanied by the insertion of counter ions from an electrolyte. From all hydroxide materials, layered nickel hydroxide is of special importance as it is the principal part of NiCd and NiMH batteries, which were the first small sealed rechargeable cells.[21] During the discharging process, the oxidation occurs at anode made of metal cadmium or metal proton-inserting alloy (MH) (Equation 1 and 2), whereas reduction occurs at nickel oxide hydroxide cathode (Equation 3).

$$Cd + 2OH^- \leftrightarrow Cd^{2+}(OH)_2 + 2e^- \quad (1)$$

$$MH + OH^- \leftrightarrow M + H_2O + e^- \quad (2)$$

$$Ni^{3+}OOH + H_2O + e^- \leftrightarrow Ni^{2+}(OH)_2 + OH^- \quad (3)$$

In recent years, Co and Mn hydroxides were also studied as potential construction materials for power cells or supercapacitors.[98] Layered nickel and cobalt hydroxides were studied as prospective materials for glucose or dopamine sensors.[99,100,101] Many studies are focused on layered hydroxides microstructure and morphology, which can significantly influence the resulting electrochemical performance.

1.6 Layered nickel and cobalt hydroxides

1.6.1 Structural aspects

Hydroxides of nickel and cobalt exist in several structural modifications.[102,103] The simplest and the most known are hydroxides with a composition $M(OH)_2$ ($M = Ni^{2+}$, Co^{2+}) possessing the closely packed brucite structure without interlayer anions. This modification is often called the β-phase (β-$Ni(OH)_2$) and in the case of nickel it is the material utilized for the industrial production of batteries. The second structural modification, the α-phase (α-$Ni(OH)_2$), possesses the structure of layered hydroxide salts with a deficit of hydroxide groups, anions in the interlayer space and large basal spacing. α-$Ni(OH)_2$ is of the LSH structural type presented in Figure 3A with Ni^{2+} ions octahedrally coordinated in the brucite-like layer. In contrast, α-$Co(OH)_2$ contains a mixture of octahedrally and tetrahedrally coordinated Co^{2+} ions as shown in Figure 3B.[104] The easy oxidation of divalent cobalt ions can lead to the structure, which contains both divalent and trivalent cobalt ions, corresponding to the monometallic LDH structure.[65] The phases containing both cobalt and nickel ions in various ratios can be also prepared possessing the structure of LDH or layered double hydroxide salts. All the structural modifications of layered nickel hydroxides are green because they contain only octahedrally coordinated divalent nickel atoms. However, the colouring of cobalt hydroxides differs by cobalt ion valency and coordination mode (Figure 6).[65,105] The octahedral β-phase is pink due to octahedral divalent cobalt, the α-phase has green or blue colour caused by tetrahedrally coordinated Co^{2+} and the Co^{2+}/Co^{3+} LDH phase is brown due to the presence of trivalent cobalt.

1.6.2 Electrochemical behaviour

Electrochemistry of Ni^{2+} and Co^{2+} hydroxides is based on reversible oxidation of divalent metal cations to corresponding oxide-hydroxides in alkaline solution.[94] The reaction is accompanied by incorporation of counter ions from electrolyte into a hydroxide electrode which is the rate determining step of the overall oxidation-reduction process.[106] Whereas the oxidation of nickel hydroxide is one electron process leading to the NiO(OH), the oxidation of cobalt hydroxides is more complex with subsequent oxidation of cobalt(3+) oxide-hydroxide to cobalt(4+) oxide.[107] The oxidation of cobalt ions occurs at a lower potential then that for nickel ions, and therefore the Co^{2+} oxidation is easier. The electrochemical reactions of nickel and cobalt hydroxides are represented by following equations:

$$Ni^{2+}(OH)_2 + OH^- \leftrightarrow Ni^{3+}OOH + H_2O + e^- \quad (4)$$

$$Co^{2+}(OH)_2 + OH^- \leftrightarrow Co^{3+}OOH + H_2O + e^- \quad (5)$$

$$Co^{3+}OOH + OH^- \leftrightarrow Co^{4+}O_2 + H_2O + e^- \quad (6)$$

The most often studied and utilized are the β-phases of Ni and Co hydroxides because they show the stable electrochemical behaviour and are available in the pure phase in the industrial scale. On the other hand, the α-phases are known for their superior electrochemical properties such as a high capacity (nearly twice higher than that for the β-phase), originating probably in their less ordered structure and turbostraticity.[108] Moreover, the expanded layered structure of the α-phase allows anion-exchange reaction and delamination which is suitable for composite or thin film fabrications.[109] However, the low stability of the α-phases in alkaline solution leads to the structural and volume changes connected with a capacity decrease which complicates the α-phase utilization.[110] The stability of the α-phase can be enhanced using doping by different transition metal ions such as Co^{2+}, Fe^{3+}, Mn^{2+}, Al^{3+} or Zn^{2+} or by dispersing nickel hydroxide in polymers or inorganic matrices.[108]

The electrochemical efficiency of layered hydroxides can be positively influenced by several ways, for example, the fabrication of composites combining layered nickel or cobalt hydroxides with graphene or carbon nanotubes enhances the overall electric conductivity and mechanical stability .[111,112,113,114] Other example is mixed nickel and cobalt hydroxide, which shows better electrochemical performance than simple hydroxides.[115] The significant increase of the electric capacity was also achieved by the utilization of nanostructural or porous materials with large surface areas.[61,116,117,118,119]

Other advantage of nanostructural Ni and Co hydroxides is possibility to construct thin electrodes acting at high scan rates. As was mentioned earlier, the electrochemical reactions of solid electrodes are accompanied by insertion of ions from electrolyte into an electrode. This slow diffusion-directed process is the rate determining step of the whole electrochemical reaction.[106]. The utilization of nanometric electrodes minimizes the diffusion of counter ions into bulk and, thus, the reaction is driven by fast charge transfer process. The usage of fast scan rates is applicable the construction of power sources with fast charging-discharging abilities.

2. Aims of the thesis

The main goal of this research work is preparation and delamination of layered nickel and cobalt hydroxides in water and the detailed characterization of prepared hydroxides and their nanosheets. The deposition of the nanosheets on conductive layers leads to the oriented films utilizable as ultrathin electrodes, which are not affected by bulk effects. In order to demonstrate the possible applications of the prepared nanosheets, they were investigated as nanoelectrodes with fast electrochemical response.

The main attention was dedicated to:

- Synthesis and characterization of nickel and cobalt layered hydroxides suitable for delamination in water.

- Delamination of prepared layered hydroxides in water to separate single-layer sheets and their detailed characterisation.

- Fabrication of thin films composed of oriented nanosheets for electrochemical studies.

3. Results and discussion

3.1 Syntheses of nickel and cobalt layered hydroxides

Initially, we focused on layered nickel hydroxides intercalated by nitrates and lactates. These hydroxides were prepared using two different approaches: LNiH-NO_3(p) and LNiH-Lac(p) were prepared by the common alkaline precipitation method and LNiH-NO_3(ae) and LNiH-Lac(ae) were prepared by anion exchange using dodecyl sulphate precursor LNiH-DS. The most effective delamination was achieved with LNiH-Lac(ae) prepared by anion exchange, therefore, the experimental conditions optimised for LNiH-Lac(ae) were used for the delamination of layered cobalt hydroxide (LCoH-Lac(ae)) and mixed layered nickel-cobalt hydroxide (LNiCoH-Lac(ae)), prepared from dodecyl sulphate precursors LCoH-DS and LNiCoH-DS, respectively. The list of prepared layered hydroxides, preparation methods, structures, and delamination ability are summarized in the Appendix 1.

Layered hydroxides LNiH-Lac(p) and LNiH-NO_3(p) prepared by direct precipitation

LNiH-Lac(p) and LNiH-NO_3(p) were prepared by direct alkaline precipitation of nickel lactate or nickel nitrate by sodium hydroxide in water at room temperature, respectively (Equation 7). This simple method yields samples of moderate crystallinity contaminated with β-$Ni(OH)_2$.

$$2Ni(A^-)_2 + 3NaOH \rightarrow Ni_2(OH)_3A^- + 3NaA^- \ (A^- = Lac^-, NO_3^-) \quad 7$$

Layered hydroxides LNiH-Lac(ae), LNiH- (NO_3)(ae), LCoH-Lac(ae) and LNiCoH-Lac(ae) prepared by anion exchange:

In order to overcome the problems with the contamination of LNiH by the β-phase, the synthesis started with the preparation of LNiH-DS, which can be obtained very pure and of good crystallinity. Then, DS anions were exchanged for nitrate or lactate anions to form LNiH-Lac(ae), LNiH-(NO_3)(ae), LCoH-Lac(ae), and LNiCoH-Lac(ae).

In the first step, LNiH-DS, LCoH-DS and LNiCoH-DS were prepared by hydrothermal precipitation of nickel and cobalt inorganic salts (Appendix 1) in the presence of SDS and HMT at 90 °C in a mixture of water and butanol (9:1). The reaction is based on thermal degradation of HMT (Equation 8) and generation of ammonia which precipitates layered hydroxides (Equation 9).

$$C_6H_{12}N_4 + 6H_2O \rightarrow 6CH_2O + 4NH_3 \qquad 8$$

$$2Ni(NO_3)_2 + NaDS + 3NH_4OH \rightarrow Ni_2(OH)_3DS + NaNO_3 + 3NH_4NO_3 \qquad 9$$

The second step was the ion exchange of DS for lactate or nitrate anions to form LNiH-Lac(ae), LNiH-(NO_3)(ae), LCoH-Lac(ae) and LNiCoH-Lac(ae). This process was achieved by the reaction of DS-intercalated hydroxide with corresponding salt (sodium lactate or nitrate) in the presence of CTABr. CTABr enhances removing DS from the interlayer gallery due to the ion-pair formation (Equation 10). The reaction was performed in a biphasic mixture of water and chloroform at the room temperature in order to accelerate the ion exchange by the dissolution of ion-pair CTA-DS in the chloroform phase.

$$Ni_2(OH)_3DS + NaLac + CTABr \rightarrow Ni_2(OH)_3Lac + CTA\text{-}DS + NaBr \qquad 10$$

3.2 Structural characterisation

The prepared layered nickel and cobalt hydroxides were characterized by various instrumental techniques. X-ray diffraction provided the basic structural information such as phase analysis, basal spacing, and information on preference orientation. FTIR and UV-vis spectroscopy revealed the chemical composition and arrangement of the hydroxide layers and interlayer anions. Thermal behaviour of prepared layered hydroxides was studied by TGA/DTA analysis combined with mass spectrometry. The chemical composition was investigated by conventional combustion elemental analysis.

3.2.1 XRD analyses

The XRD patterns of all prepared hydroxides (Figures 8, 9) show typical diffractions of layered simple hydroxides. The first basal diffraction can be found in the range between 8 and 30 Å corresponding to the interlayer spacing, which is dependent on the type of intercalated anion (Table 2). The most intensive basal maxima can be found below 20° (2θ). Nonbasal diffractions of all prepared hydroxides can be found at typical positions around 34, and 60° (2θ).

Table 2. Basal spacings of prepared layered hydroxides. [120,121,122]

Layered hydroxide	Basal spacing [Å]
LNiH-Lac(p)	10.5
LNiH-NO_3(p)	8.1
LNiH-DS	27.2
LCoH-DS	19.1
LNiCoH-DS	22.0
LNiH-Lac(ae)	10.5
LNiH-NO_3(ae)	10.0
LCoH-Lac(ae)	11.8
LNiCoH-Lac(ae)	9.5

The basal diffractions of LNiH-NO_3(p) and LNiH-Lac(p) (Figure 8A, B) are considerably broadened in comparison with all samples prepared by hydrothermal precipitation or anion exchange, which is caused by lower crystallinity of the directly precipitated samples. Moreover, the alkaline precipitation leads to the β-phase formation documented by broad diffraction peaks at 38° (2θ).

Layered hydroxides intercalated with DS, i.e., LNiH-DS, LCoH-DS, and LNiCoH-DS, have basal spacings ranging from 19 to 27 Å, which is in accordance with effects of the intercalated bulky anions (Figure 9). The differences in basal spacings are caused mainly by different arrangement of DS and varying content of water molecules in the interlayer space. The crystallinity of these samples is significantly greater than that of directly precipitated hydroxides as documented by a set of sharp basal diffractions. The XRD patterns of DS-intercalated layered hydroxides also show that no β-phase is formed during hydrothermal precipitation.

Upon anion exchange of DS for lactate, the basal spacings are shifted to lower values in comparison with corresponding dodecyl sulphate precursors, documenting successful intercalation of lactate anions (Table 2). The differences in the basal spacings of LNiH-NO_3(p) and LNiH-NO_3(ae) are caused by different arrangements of nitrate anions within the hydroxide interlayer as also documented by FTIR spectroscopy. The good crystallinity of anion-exchanged hydroxides is preserved and no β-phase was detected by XRD analysis.

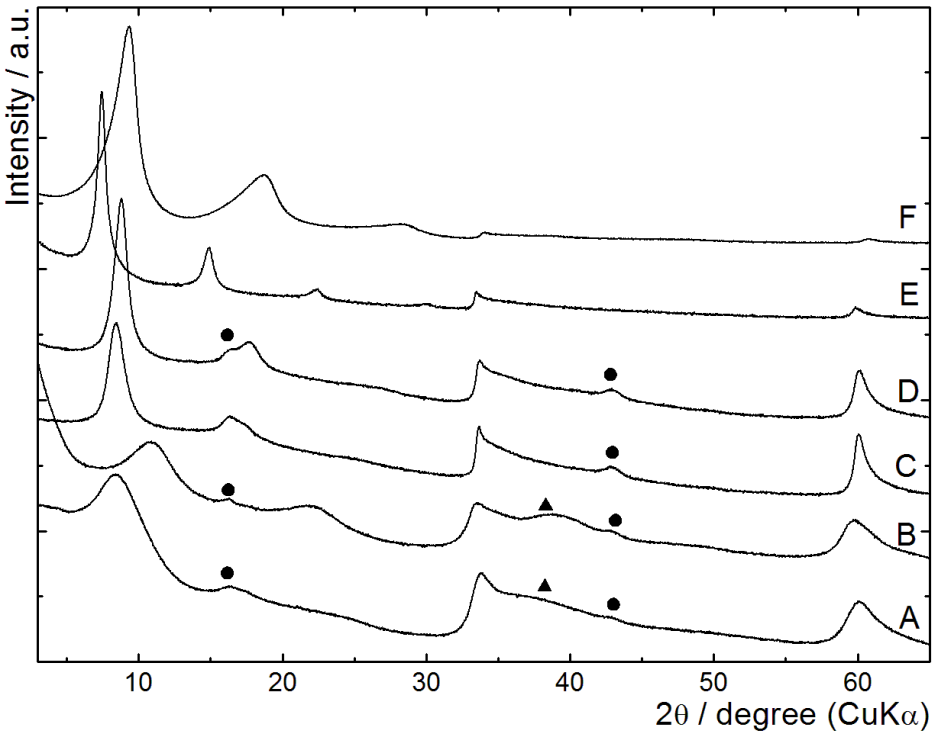

Figure 8. XRD patterns of LNiH-Lac(p) (A), LNiH-NO_3(p) (B), LNiH-Lac(ae) (C), LNiH-NO_3(ae) (D), LCoH-Lac(ae) (E), LNiCoH-Lac(ae) (F). Mylar foil support (●) and β-phase impurity (▲) are labelled. The curves are vertically shifted for better clarity.

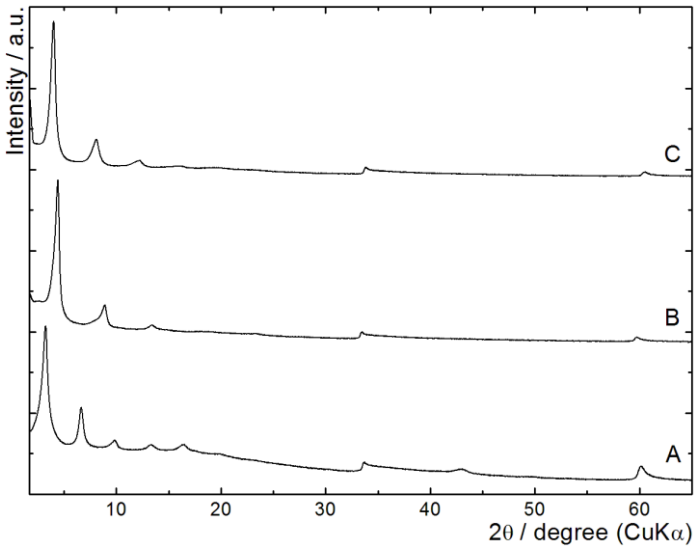

Figure 9. XRD patterns of LNH-DS (A), LCoH-DS (B) and LNiCoH-DS (C). The curves are vertically shifted for better clarity.

3.2.2 FTIR spectrometry

FTIR spectra of all prepared layered hydroxides display typical bands of water molecules represented by a broad band around 3500 cm^{-1} (a) corresponding to the stretching vibrations of O-H groups, and a peak between 1600 and 1640 cm^{-1} (c) corresponding to the deformation vibration. The skeletal vibrations of the hydroxide layers can be found as a broad composite band approximately at 600 cm^{-1} (j). Additional bands are caused by the intercalated anions.

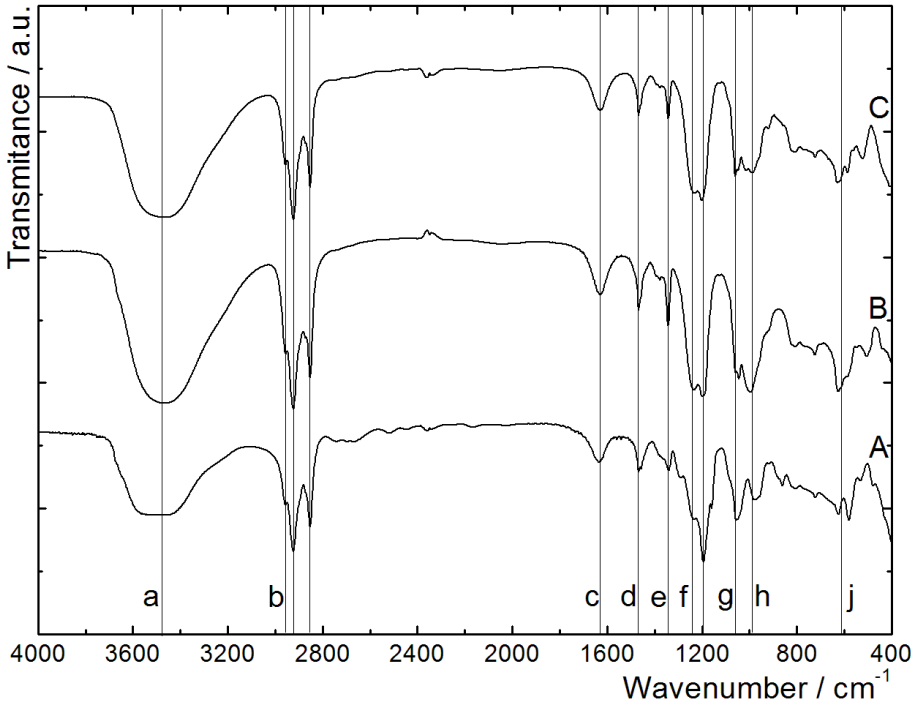

Figure 10. FTIR spectra of LNiH-DS (A), LCoH-DS (B) and LNiCoH-DS (C).

The FTIR spectra of LNiH-DS, LCoH-DS and LNiCoH-DS (Figure 10A, B, C) contain the characteristic bands of DS anions. The group of sharp peaks between 3000-2800 cm^{-1} (b) corresponds to the C-H stretching vibrations, and the C-H bending vibration can be found at 1468 cm^{-1} (d). The sulphate groups have typical vibrations at approximately 1230 (f), 1200 (g) and 1050 cm^{-1} (h). All samples are contaminated by a small amount of HMT documented by the peak at 1340 cm^{-1} (e).

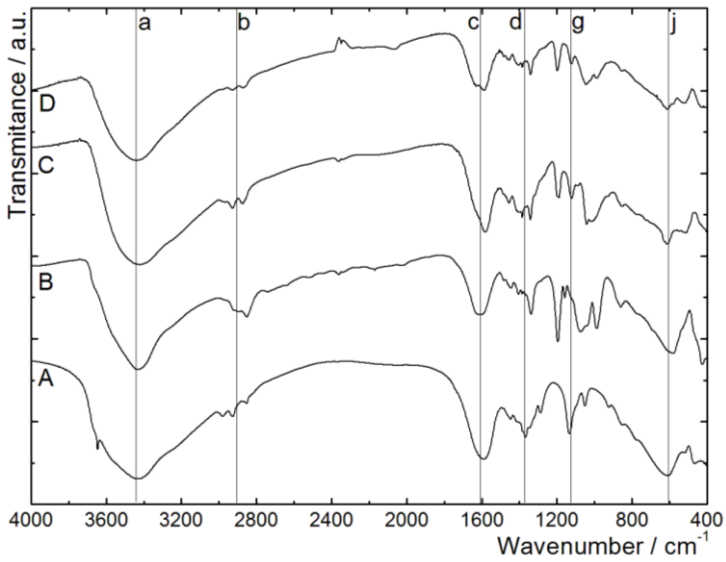

Figure 11. FTIR spectra of layered hydroxide lactates: A) LNiH-Lac(p), B) LNiH-Lac(ae), C) LCoH-Lac(ae), D) LNiCoH-Lac(ae).

The FTIR spectra of LNiH-Lac(p), LNiH-Lac(ae), LCoH-Lac(ae), LNiCoH-Lac(ae) (Figure 11) contain bands of lactate anions. The group of maxima between 3000–2800 cm^{-1} (b) can be assigned to C-H vibrations. Antisymmetric vibration of coordinated carbonyl group in carboxylate complexes is generally in the area between 1550 and 1630 cm^{-1} and in this case is partially obscured with water stretching vibration at the area between 1600 and 1640 cm^{-1}, merging into one broad band at approximately 1600 cm^{-1}(c). The corresponding symmetric vibration band is at 1367 cm^{-1} for LNiH-Lac(p), the bands of anion-exchanged lactates are in the area between 1350 and 1410 cm^{-1} partially obscured by bands of HMT and DS impurities (d) and thus it is difficult to determine the precise value of wavenumber. The C-OH stretching vibration (g) of lactate anions are in the area around 1130 cm^{-1} (Table 3).

Table 3. Asymmetric (ν_{as}) and symmetric (ν_s) stretching modes of the lactate carboxyl group, and the stretching C-OH vibrations in layered hydroxide lactates.[120,121,122]

Layered hydroxide	CO ν_{as} (c) [cm^{-1}]	CO ν_s (d) [cm^{-1}]	ν C-OH (g) [cm^{-1}]
LNiH-Lac(p)	1592	1367	1134
LNiH-Lac(ae)	1602	~1350	1125
LCoH-Lac(ae)	1577	~1405	1122
LNiCoH-Lac(ae)	1587	~1402	1122

Nitrate anions (Figure 12) of LNiH-NO_3(p) are represented by four vibration bands at 1495 (d), 1384 (e), 1300 (g) and 993 cm^{-1}(i). The peak (e) can be assigned to the N-O stretching vibration of free nitrate anions ($C3_v$ symmetry), whereas the peaks (d), (g) and (i) correspond to the vibrations of coordinated NO_3^- ion ($C2_v$ symmetry), suggesting that LNH-NO_3(p) contains both free and coordinate nitrate anions. On the other hand, the FTIR spectra of LNH-NO_3(ae) contain only the peak (e), suggesting that mostly free nitrate anions are present. These differences correlate well with the different basal spacing of anion-exchanged and precipitated layered hydroxide nitrates. Analogously to LNiH-Lac(ae), the FTIR spectrum of LNiH-NO_3(ae) contains signals of HMT (g) and DS (h).

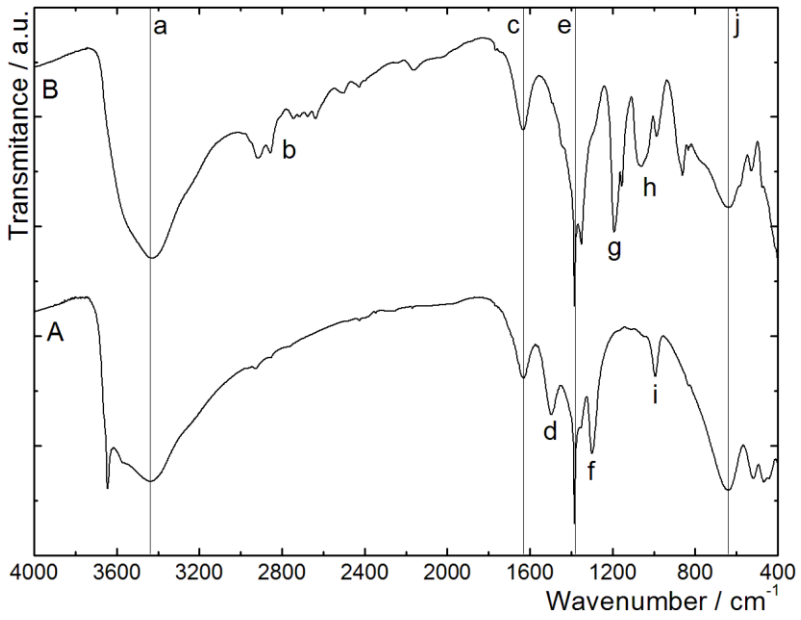

Figure 12. FTIR spectra of LNiH-NO_3(p) (A) and LNiH-NO_3(ae) (B).

3.2.3 UV-Vis spectrometry

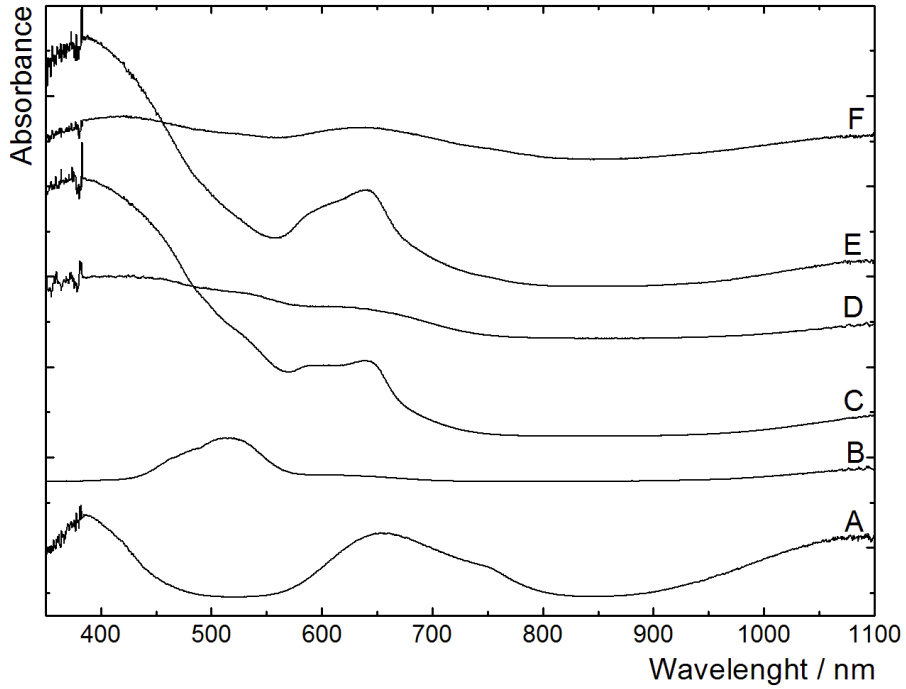

Figure 13. Absorption spectra of LNiH-Lac(ae) (A), $Co(Lac)_2$ (B), LCoH-DS (C) and LCoH-Lac(ae) (D), LNiCoH-DS (E) and LNiCoH-Lac(ae) (F).

Due to the high stability of the Ni^{2+} oxidation state and the octahedral coordination, UV-Vis spectra of the layered nickel hydroxides contain typical absorption bands of octahedrally coordinated Ni^{2+} ions (Figure 13A), resulting in green colour of all LNiH samples. The bands of Ni^{2+} in the LNiCoH-DS and LNiCoH-Lac spectra are poorly recognized due to their low absorption coefficients in the comparison with the absorption bands of tetrahedral Co^{2+}.

Table 4. UV-Vis transitions of octahedrally coordinated Ni^{2+} of layered nickel hydroxides.[120,121,122]

Transition	Wavelength [nm]
$^3A_{2g}(F) \rightarrow {}^3T_{1g}(P)$	383
$^3A_{2g}(F) \rightarrow {}^1E_g(G)$	658
$^3A_{2g}(F) \rightarrow {}^3T_{1g}(F)$	ca 750 (shoulder)

Cobalt in layered hydroxides can exist in several oxidation states and coordination modes, which are distinguishable by UV-Vis spectroscopy (Figure 6). All of the prepared cobalt hydroxides contain octahedrally coordinated Co^{2+} with typical absorption band corresponding to the $4T_{1g}(F) \rightarrow 4T_{1g}(P)$ transition at 515 nm (Figure 13B), causing typical pink colour (e.g., β-$Co(OH)_2$).Tetrahedrally coordinated Co^{2+} in the spectrum of LCoH-DS and LNiCoH-DS can be evidenced by absorption bands corresponding to the $4A_2 \rightarrow 4T_1(P)$ transition at 639 nm. This band is typically several orders of magnitude stronger than that of octahedral Co^{2+} and, therefore, the layered hydroxides containing tetrahedral Co^{2+} ions are typically blue or green (Figure 13C, E). Prepared LCoH-DS is beige suggesting the partial oxidation of Co^{2+} to Co^{3+} as was evidenced by average oxidation state determined by volumetric iodometric titrations. The partial oxidation of Co^{2+} is also present in LNiCoH-DS, but the green colour of this sample is caused by the presence of octahedral Ni^{2+}. The presence of Co^{3+} ions together with tetrahedral Co^{2+} atoms suggests that both cobalt containing layered hydroxides intercalated with DS are mixtures of the LHS/LDH phases.

UV-Vis spectra of LCoH-Lac(ae) and LNiCoH-Lac(ae) (Figure 13D, F) differ significantly from their parent dodecyl sulphate precursors. The band of tetrahedral cobalt disappeared during anion exchange and the spectra contain broad and subtle bands in the area between 400 and 500nm, and 550 and 650 nm, because of partial oxidation of Co^{2+} ions, suggesting the LDH structure of LCoH-Lac(ae) and LNiCoH-Lac(ae). The resulting colour of LCoH-Lac(ae) is brownish, which is typical of octahedral Co^{3+}, whereas LNiCoH-Lac is green-brown due to the contribution of octahedral Ni^{2+} cations.

3.2.4 DTA/TGA analysis

DTA curves of all prepared layered hydroxides show typical endothermic peaks, corresponding to the release of surface and interlayer water approximately at 100°C. The mass reduction connected with this peak was used for estimation of the water content (Table 5.).

Table 5. Water content (n) per one metal ion estimated from the mass loss during thermal analyses.[120,121,122]

Layered hydroxide	Mass loss at 100 °C [%]	n H_2O
LNiH-Lac(p)	13.1	1.0
LNiH-NO_3(p)	6.8	0.47
LNiH-DS	7.0	0.70
LNiH-Lac(ae)	7.7	0.53
LNiH-NO_3(ae)	7.9	0.54
LCoH-DS	4.7	0.49
LCoH-Lac(ae)	8.8	0.70
LNiCoH-DS	5.7	0.62
LNiCoH-Lac(ae)	8.1	0.65

The second step, corresponding to decomposition of the hydroxide layers and interlayer anions, is connected with the extensive mass loss and release of gases. This step in the dodecyl sulphate-intercalated layered hydroxides can be found between 200 and 600°C and is accompanied by the release of CO_2 and H_2O. The anion degradation ends between 770 and 790 °C and is indicated by the release of SO_x. The decomposition of lactates and nitrates is accompanied by H_2O, CO_2 and NO_x release between 200 and 400°C.

The TGA/DTA curves of LCoH-DS and LCoH-Lac(ae) contain endothermic peak approximately at 920°C assigned to the phase transition of spinel Co_3O_4 to cubic CoO, which is typical for cobalt oxides. This peak is missing in the TGA/DTA curves of LNiCoH-DS and LNiCoH-Lac(ae), indicating that Ni and Co cations are homogeneously distributed, forming a mixed oxide rather than the mixture of respective oxides.

3.2.5 Elemental composition

The nickel and cobalt content was determined by ICP-MS spectrometry and the CHN and S analyses were measured by a standard combustion technique (Table 6).

Table 6. Co content, valency and proposed composition of cobalt-containing hydroxides. The suggested formulas were determined by the combination of combustion elemental analysis, ICP-MS spectrometry, and iodometric titration.[120,121,122]

Layered hydroxide	Co content [%]	Ni:Co ratio	Co valency	Suggested formula
LCoH-DS	31.43	-	2.23	$(Co^{2+})_{0.77}(Co^{3+})_{0.23}(OH)_{1.98}(DS)_{0.25}(HMT)_{0.07} \cdot 0.5\ H_2O$
LCoH-Lac(ae)	41.85	-	2.23	$(Co^{2+})_{0.76}(Co^{3+})_{0.24}(OH)_2(Lac)_{0.24}(HMT)_{0.07} \cdot 0.7H_2O$
LNiCoH-DS	10.47	65:35	2.66	$Ni_{0.65}(Co^{2+})_{0.12}(Co^{3+})_{0.23}(OH)_{1.92}(DS)_{0.3}(HMT)_{0.05} \cdot 0.6\ H_2O$
LNiCoH-Lac(ae)	13.61	67:33	2.73	$Ni_{0.67}(Co^{2+})_{0.09}(Co^{3+})_{0.24}(OH)_2(Lac)_{0.19}(DS)_{0.03}(HMT)_{0.06} \cdot 0.7\ H_2O$

3.3 Delamination

Delamination of LNiH-Lac(p) and LNiH-NO_3(p) was achieved by shaking the wet product in deionized water overnight (approximately 20 h) at room temperature. Both materials delaminate quantitatively, forming colloid suspensions with concentrations up to 30 $mg \cdot mL^{-1}$.

LNiH-Lac(ae), LCoH-Lac(ae) and LNiCoH-Lac(ae) delaminate spontaneously and quantitatively during the anion exchange reaction after removing the chloroform phase with DS-CTA ion pairs (Eq. 10) from the reaction mixture. From all prepared layered hydroxides, LNiH-Lac(ae), LCoH-Lac(ae) and LNiCoH-Lac(ae) show the best delamination ability, which can be caused by the absence of the β-phase in the final products, high polarity and solubility of lactate anions. The efficient removing of DS during anion exchange supported by the DS-CTA ion pair formation plays also an important role. The prepared colloid dispersions reach the concentrations up to 30 $mg \cdot mL^{-1}$ (Figure 14A, B, C). At higher concentrations, the nanosheet dispersions form gels (Figure 14D).

The delamination of LNiH-NO_3(ae) was not successful, probably due to compact layer stacking, evidenced by XRD and FTIR.

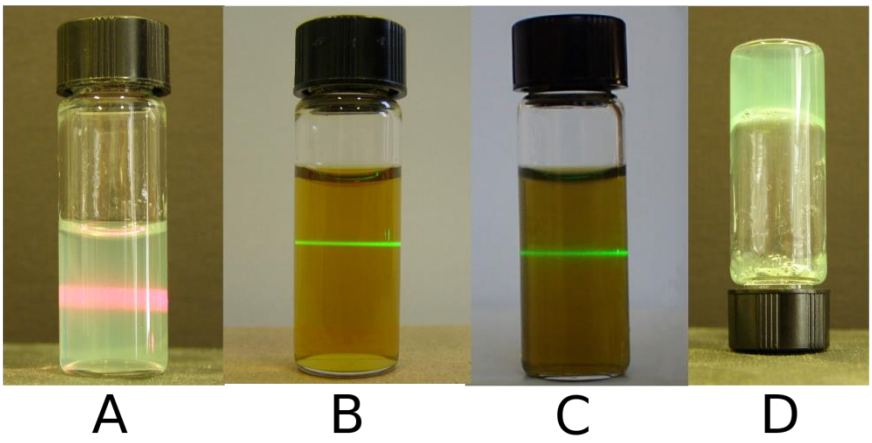

Figure 14. Colloid dispersions of LNiH-Lac(ae) (A), LCoH-Lac (B), LNiCoH-Lac (C), and LNiH-Lac nanosheet gel (D). The Tyndall effect is documented by a laser pointer.

Hydroxide nanosheet colloids were evaporated on a mylar foil at room temperature to form self-standing films (Figure 15.), which display strong preferential orientation due to the self-assembling ability of the planar hydroxide nanosheets, as is documented by XRD patterns measured in reflection and transmission mode (Figure 16). The basal 00l diffractions are present only in reflection mode (Figure 16B), whereas the only nonbasal diffractions can be found in transmission mode (Figure 16C).

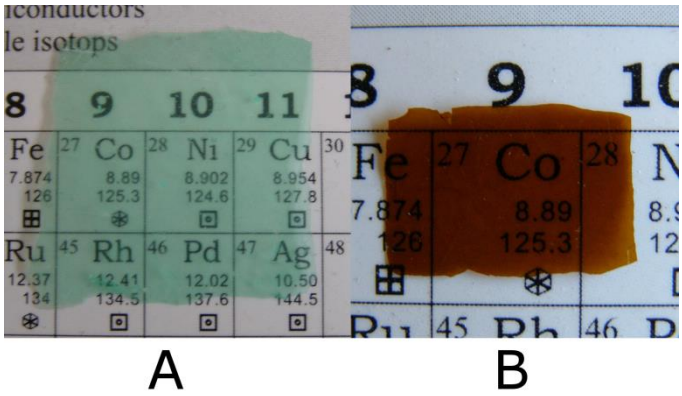

Figure 15. Self-standing films made from LNiH-Lac(ae) (A) and LCoH-Lac(ae) (B).

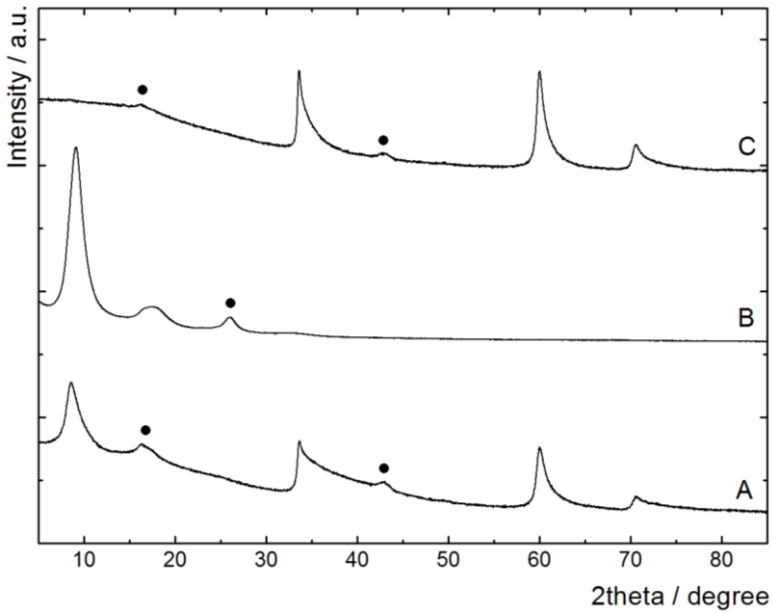

Figure 16. Powder XRD patterns documenting the preferential orientation of LNiH-Lac(ae): A) powder sample, B) reflection mode of drop-casted film, C) transmission mode of the same film. Mylar foil support is labelled (●).The curves are vertically shifted for better clarity.

3.4 The structural characterisation of hydroxide nanosheets

The nanosheet dispersions were characterized by SAXS in order to investigate their shape and dimension. AFM was used for determination of the thickness of the nanosheets deposited on mica and graphite surfaces. TEM observations were employed for studying nanosheet lateral dimensions.

3.4.1 Small angle X-ray scattering (SAXS)

The scattering curves were measured in the range of q between 0.005-1.1 $Å^{-1}$ ($q = (4\pi/\lambda)\sin\theta$) corresponding to the 2θ range of 0.07-15.5°. The obtained scattering curves follow the empirical equation $I(q) = Aq^{-\alpha} + B$, where I is the scattering intensity, $Aq^{-\alpha}$ describes the scattering by homogenous particles and B is proportional to particle concentration. Exponent α was equal to 2 which is typical of planar particles.

The scattering curves of diluted colloid dispersions (4 mg mL^{-1}) did not contain any diffraction maxima, evidencing the presence of single-layer nanosheets. The thickness, derived from the scattering curves of LNiH-Lac(ae), LNiH-Lac(p), LCoH-Lac(ae) and LNiCoH-Lac(ae) colloids, were smaller than 1 nm. The thickness of the hydroxide nanosheets prepared from LNiH-NO_3(p) was between 3 – 6 nm. In all cases, the lateral dimensions of the nanosheets exceeded 50 nm (Table 7). The scattering curves of dense gel-like colloid dispersions showed diffraction maxima at 0.57 A^{-1} (d_{001} = 11 Å) and thickness of nanosheets was between 2 – 4 nm, suggesting the formation of aggregates made of 2 – 3 hydroxide layers.

Table 7. Dimensions of the hydroxide nanosheets prepared from indicated layered hydroxides as obtained using SAXS.[120,121,122]

Layered hydroxide	Thickness / nm	Lateral dimension /nm
LNiH-Lac(ae)	0.5	55
LNiH-Lac(p)	0.7	80
LNiH-NO_3(p)	3 – 6	75
LCoH-Lac(ae)	0.7 – 0.9	70
LNiCoH-Lac(ae)	0.7	50

3.4.2 Atomic force microscopy (AFM)

The samples for AFM were prepared by spin-coating of diluted nanosheet colloid dispersions on a mica surface. The AFM images of nickel and cobalt hydroxide nanosheets revealed side-by-side aggregates of the nanosheets approximately 1 nm thick, documenting the formation of ultrathin single-sheet layers (Figure 17). In the case of LNiH-Lac(ae) and LNiH-Lac(p), bigger thicknesses were also visible due to the vertical nanosheet stacking. The roughness factors Ra calculated from the area of 500 x 500 nm were up to 0.3 nm, documenting the very smooth coverage of the surface.

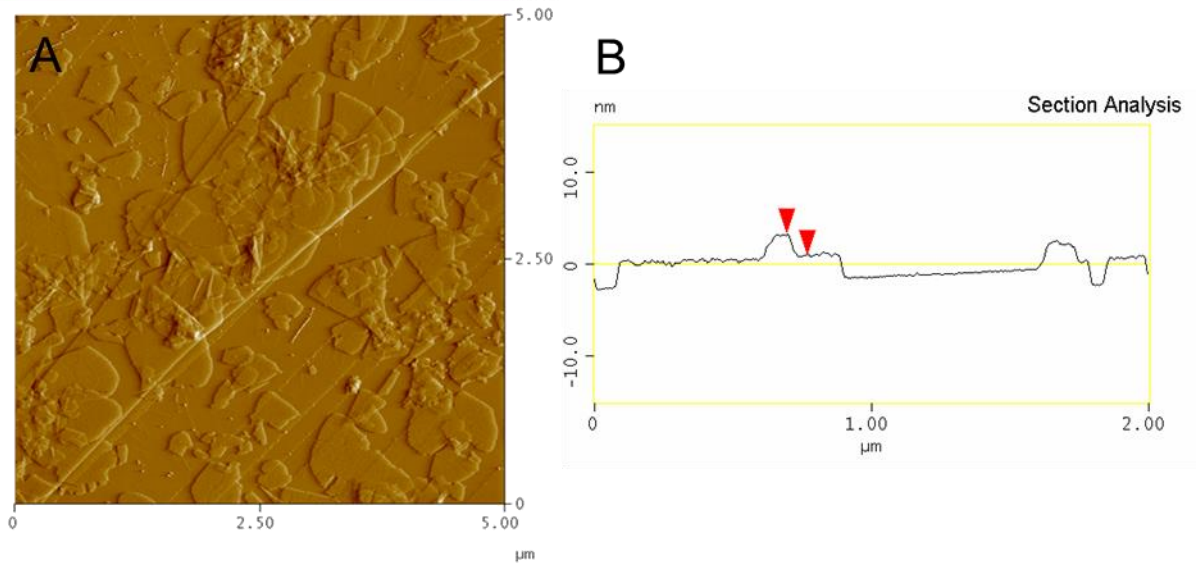

Figure 17. 2D aggregates of the nickel-cobalt hydroxide nanosheets spin-coated on the basal plane of HOPG: AFM (tapping) topography (A); profile (line) analysis (B). Red arrows indicate a thickness of 2.5 nm.[122]

3.4.3 Transmission electron microscopy (TEM)

Layered nickel hydroxides were studied by TEM to determine the shape, lateral size and composition of the prepared nanosheets. LNiH-NO_3(p) forms hexagonal single-crystalline nanosheets with a lateral size between 50 and 90 nm, which is in good agreement with the results obtained from SAXS (Figure 18). Unfortunately, the nanosheets of LNiH-Lac(p) and LNiH-Lac(ae) were unstable under electron beam, forming metal nickel nanoparticles. In order to stabilize the nanosheets, LNiH-Lac(ae) was protected by freezing in the ethane matrix. The TEM images of the protected sample reveal nanosheets with a lateral dimension of approximately 100 nm (Figure 19). The nanosheets appear to be composed of several crystals as can be seen in electron diffraction image. The electron diffraction corresponds to nickel hydroxide and nickel oxide, suggesting partial degradation of the sample under electron beam.

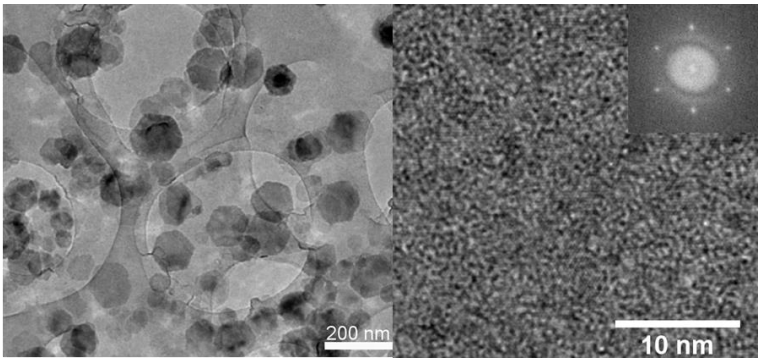

Figure 18. TEM images of LNiH-NO_3(p) nanosheets (left). The electron diffraction of the selected area evidences the monocrystalline nature of the nanosheets (right).[120]

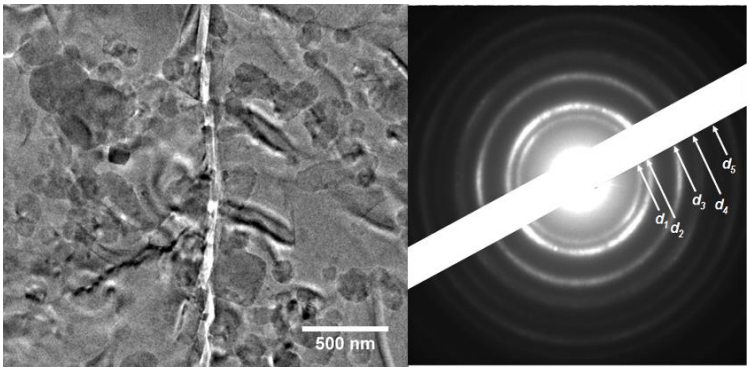

Figure 19. TEM images of protected LNiH-Lac(ae). The nanosheets are composed of microcrystalline grains. The corresponding SAED patterns:d_1 = 2.45±0.05Å, d_2 = 2.10±0.05Å, d_3 = 1.50±0.05Å, d_4 = 1.30±0.05Å, d_5 = 1.20±0.05Å.[120]

3.5 Electrochemical study

In order to evaluate the electrochemical responses of the hydroxide nanosheets, we analysed nanomorphology and cyclic voltammograms of deposited hydroxide nanosheets in cooperation with Pavel Janda from J. Heyrovský Institute of Physical Chemistry of the Czech Academy of Sciences (Figure 20 and Figures hereafter). The obtained results are interpreted as follows.

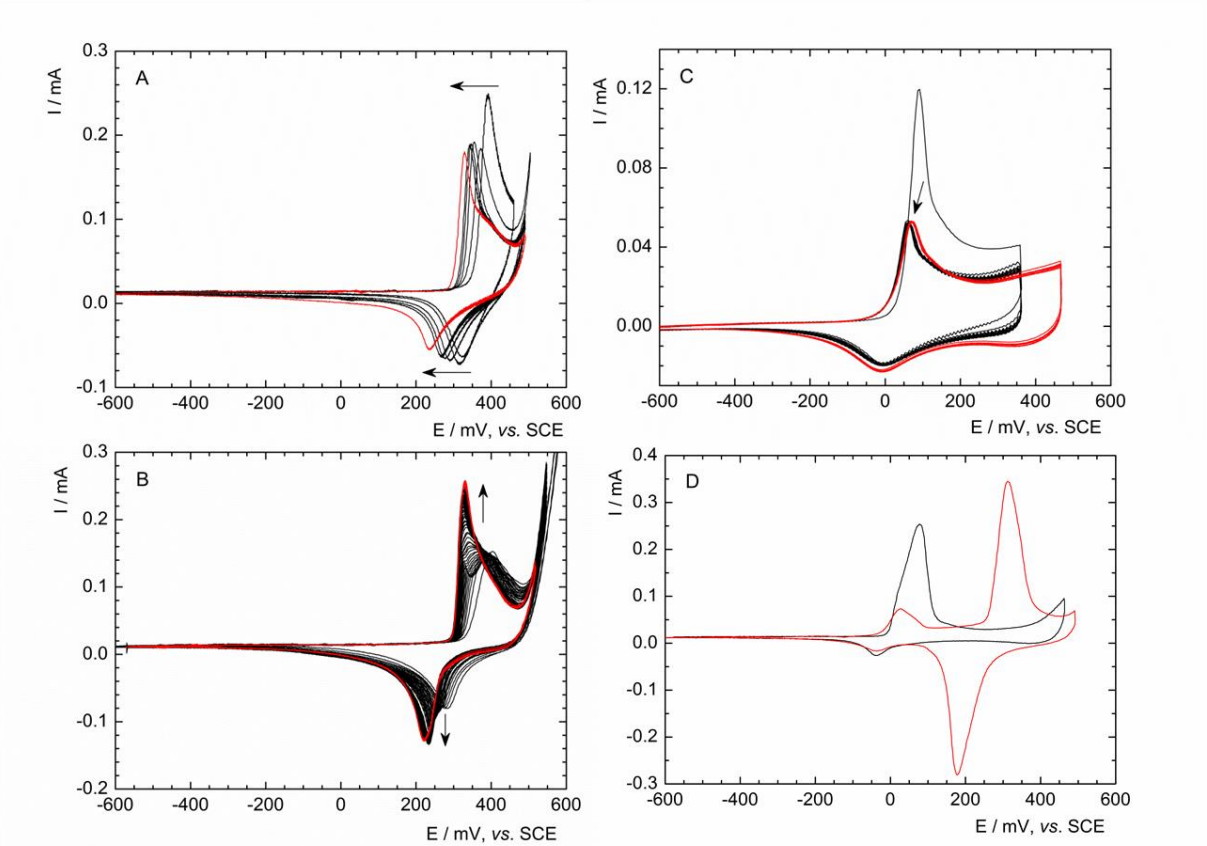

Figure 20. CV curves of nickel-cobalt hydroxide nanosheets (A), nickel hydroxide nanosheets (B), cobalt hydroxide nanosheets (C) mixed nickel hydroxide and cobalt hydroxide nanosheets (1:1) (D). The arrows show the shifts of the peaks during cycling (black) to the steady-state voltammogram after 40–50 cycles (red). Scan rate v = 100 mV s^{-1}, aqueous 1 M KOH deoxygenated by argon, SCE reference electrode.[122]

3.5.1 Electrochemical study of nickel hydroxide nanosheets[120]

The spin coated deposit was prepared by spin coating of 2 $mg \cdot mL^{-1}$ solution of the LNiH-Lac(ae) nanosheets. The mass of spin coated deposit was not possible to determine due to its low thickness.

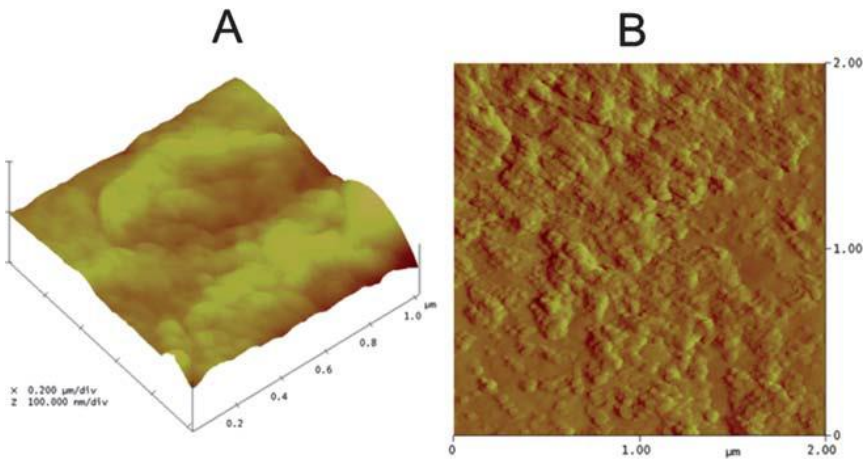

Figure 21. AFM topography (tapping) image of a nickel hydroxide film drop-casted on HOPG prepared from an aqueous dispersion of the LNH–lactate (ae) nanosheets before (A) and after (B) repetitive potential cycling (50 cycles from 150 mV to +500 mV vs. SCE reference electrode, 1 M KOH electrolyte). The columnar stacking of lamellae after potential sweeping is well resolved.[120]

The voltammetric curves of nickel hydroxide nanosheets (Figure 20B) shows significant increase of electrochemical charge transfer efficiency and ionic conductivity during the first 50 cycles accompanied by structural rearrangement which is visible in the AFM images of electrode before and after CV measurement (Figure 21). Structural changes are probably caused by incorporation of counter ions from the electrolyte into the electrode. After the first 100 cycles, the reaction reaches the steady state. Structural changes are characteristic for α-$Ni(OH)_2$ and it is often explained as the substitution of OH^- ions for intercalated anions. This process is usually accompanied by a significant loss of the electrochemical efficiency, but surprisingly, this was not observed in our case.

The whole electrochemical reaction is apparently reversible, the anodic peak corresponds to oxidation of the hydroxide nanosheets to NiO(OH) and the cathodic peak is connected with the reverse process (Equation 4). The charge reversibility of the electrochemical reaction was expressed as the ratio of anodic and cathodic charges (Q_a/O_c). This ratio decreases by approximately 50 % as the scan rate increased to 50 mV s^{-1}, suggesting the significant influence of ion diffusion. This indicates that electrode contains a rather thicker layer composed of the nanosheets.

3.5.2 Electrochemical study of cobalt hydroxide nanosheets[121]

The electrodes made of the cobalt hydroxide nanosheets were prepared by drop casting and spin coating methods. The spin-coated electrodes were prepared using 2 mg mL^{-1} or 10 mg mL^{-1} dispersions in order to evaluate the effects of the different thicknesses of the deposits. The drop-casted electrode was prepared using 2mg mL^{-1} dispersion.

The morphology of the electrodes was studied by AFM before and after cyclic voltammetry measurements. The spin-coated deposits, prepared using 2 and 10 mg mL^{-1} dispersions (Figure 22), display relatively smooth surfaces with roughness parameters Ra of 1.6 and 5.4 nm, respectively, and exhibit a quasi-two-dimensional nanosheet structure with a uniform sheet thickness of approximately 2.5 nm. Drop casting the 2 mg mL^{-1} dispersion yields uneven and rough surfaces with Ra of approximately 16 nm and unresolved platelet nanostructures.

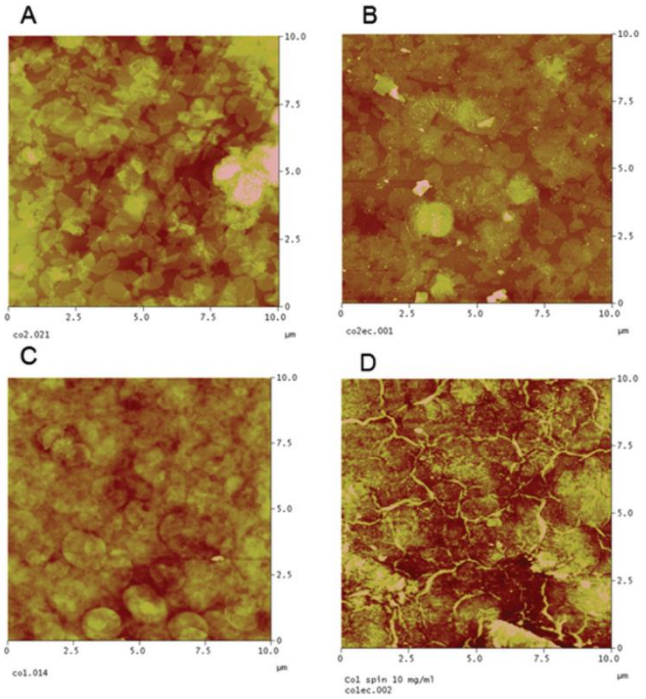

Figure 22. AFM images of cobalt hydroxide nanosheets spin-coated on HOPG: prepared from 2mg mL^{-1} dispersion before (A) and after (B) repetitive voltammetric cycling; prepared from 10 mg mL^{-1} dispersion before (C) and after (D) repetitive voltammetric cycling.[121]

The CV curves of spin-coated deposits show three pairs of peaks (Figure 23). The first anodic peak (at 0 mV vs. SCE) is attributed to oxidation of the $Co(OH)_2$ nanosheets to form cobalt oxyhydroxide, CoOOH, and the cathodic peak corresponds to the reverse reduction process at the interface between the cobalt hydroxide nanosheets and the electrolyte (Figure 23A, peak 1; Equation 5). The second peak at approximately 70 mV vs. SCE, indicating the formation of distinct phases with different electrode kinetics, is almost absent for the deposits prepared using the 2 mg mL^{-1} dispersion (Figure 23A, peak 2). The appearance of the second peak may be related to a nanomorphological rearrangement and/or phase change in the deposit bulk that would be logically more pronounced in denser deposits prepared using the 10 mg mL^{-1} dispersion. Third peak at 400 mVs^{-1} can be assigned to the further oxidation of CoO(OH) to CoO_2 (Figure 23A, peak 3; Equation 6) documenting easier oxidation and richer scale of Co oxidation states in the comparison with nickel hydroxide nanosheets. The peaks in the CV curve of drop casted electrodes are unresolved and merging together, which is probably caused by slow ion diffusion inside the bulky electrode (Figure 23B).

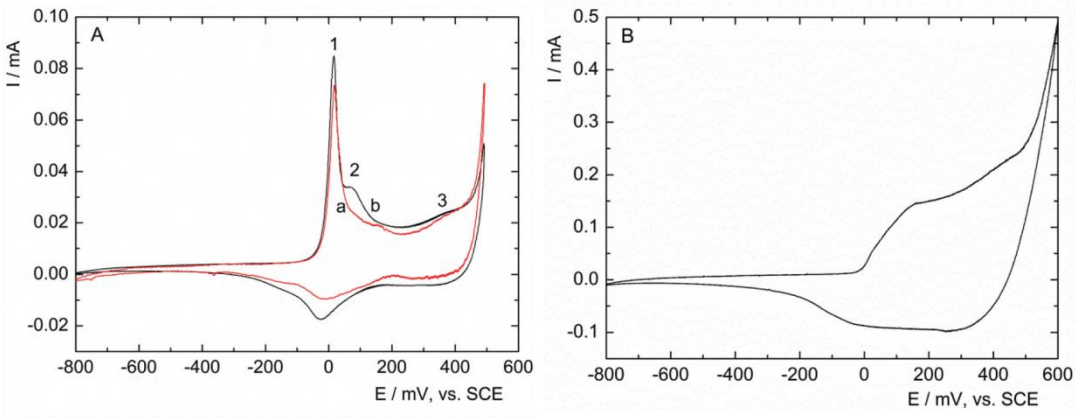

Figure 23. Cyclic voltammetry of cobalt hydroxide deposits on the basal plane HOPG: (A) spin-coated deposits prepared using 2 mg mL^{-1} (a) and 10 mg mL^{-1} (b) dispersions (for better clarity, the current of deposit (a) was multiplied by 10); (B) drop-cast deposit prepared from the 2 mg mL^{-1} dispersion. Cyclic voltammetry was performed in aqueous 1 M KOH electrolyte solution deoxygenated with argon. The scan rate was 10 mV s^{-1}. The numbering of the peaks corresponds to the discussion in the text.[121]

The charge efficiency of the electrochemical reaction expressed as the Q_a/Q_c ratio oscillates between 0.8 and 1.2 and it is independent on scan rate up to 200 mV s^{-1}. This excellent charge transfer efficiency at very high scan rates is due to the nanometric thickness of the nanosheets deposit. This is further evidenced by AFM analyses, showing the single separated nanosheets covering the HOPG surface.

3.5.3 Electrochemical study of nickel-cobalt hydroxide nanosheets[122]

These electrodes were prepared using 2mg mL^{-1} nanosheet dispersions by spin coating on the HOPG surface. The AFM images shows side-by-side aggregates of the nanosheets with a thickness of 2.5 nm. This electrode morphology is principal for an investigation of single nanosheet electrochemistry free of effects caused by the bulk material.

Cyclic voltammetry of the nanosheets shows, after an anomalous anodic peak at approximately +400 mV during the first sweep, a steady shift of both peak potentials towards values similar to the redox reaction of the pure nickel hydroxide nanosheets at approximately E_P = +220 mV/+310 mV (Figure 20A, B). This behaviour contrasts with the single nickel hydroxide nanosheets exhibiting a considerable rearrangement during the first several sweeps towards more efficient charge transfer. For comparison, the voltammetry of the cobalt hydroxide nanosheets is characterized by the first anomalous scan, which is followed by a charge drop to the steady state at approximately 30% of the original peak magnitude (Figure 20C). These changes can be explained by the layer instability upon redox sweeping.

Whereas peak potentials of the nickel-cobalt hydroxide nanosheets reflect a redox behaviour of the nickel hydroxide nanosheets, peak currents, which are fully developed already from the first potential scan, resemble the behaviour of the cobalt hydroxide nanosheets. Therefore, the slow reorganization occurring during the initial sweeps of the nickel hydroxide nanosheets is missing. The current drop observed between the first and subsequent peaks is milder than in the case of the monometallic cobalt hydroxide nanosheets (Figure 20C).

For comparison, voltammetric curves of deposited mixtures of the nickel hydroxide and cobalt hydroxide nanosheets show considerably different behaviour than the nickel-cobalt hydroxide nanosheets (Figure 20A, D). The peak couple at E_P = -45 mV/+50 mV during the first sweep corresponds to the cobalt hydroxide redox reaction (Equation 5). The current of the couple significantly decreases with continuous cycling, whereas a new peak couple, ascribed to the separated nickel hydroxide nanosheets, develops at E_P = +200 mV/+345 mV (Equation 4). Evidently, these voltammetric curves reflect the behaviour of the respective hydroxide nanosheets.

The observed significant influence of both metals in the double metal hydroxide nanosheets can be ascribed to mutual compensation of the cobalt and nickel response via electron sharing between these metals in the hydroxide nanosheets. Considering a one-electron reaction, the charge of approximately 100 mC exchanged in the electrochemical redox reaction (Figure 20A) matches well (in order of magnitude) to the number of Co and Ni active centres found on the electrode by elemental analysis. This finding indicates the participation of a majority of the active centres in the charge exchange reaction.

4. Conclusion

A series of layered hydroxides was prepared by alkaline precipitation, hydrothermal precipitation and anion exchange. Some of them (LNiH-NO_3(p), LNiH-Lac(p), LNiH-Lac(ae), LCoH-Lac(ae) and LNiCoH-Lac(ae)) were successfully delaminated in water under mild conditions. The delamination was quantitative and dense nanosheet dispersions had concentrations up to 30 $mg \cdot mL^{-1}$. These colloid dispersions contained single layer sheets of a nanometric thickness as evidenced by SAXS and AFM. The prepared colloid dispersions were successfully used for the deposition of the hydroxide nanosheets. Thus, the hydroxide nanosheets made of LNiH-Lac(ae), LCoH-Lac(ae) and LNiCoH-Lac(ae) were used for the fabrication of thin-electrodes by spin coating and their electrochemical performance was analysed by cyclic voltammetry at different sweep rates.

The results can be summarized as follows:

1) Delamination of layered hydroxides in aqueous solution is favoured by intercalation of polar and highly water-soluble anions such as lactate. Our published paper was the first to prove the real delamination of layered nickel hydroxide into respective hydroxide nanosheets in water.

2) The anion arrangement can influence delamination capability which was documented by the absence of delamination of more crystalline and tightly-packed LNiH-NO_3(ae).

3) Hydrothermal precipitation leads to the products with good crystallinity and the absence of the β-phase. This method is more convenient than direct precipitation for the fabrication of phase-pure hydroxide materials of high crystallinity.

4) Cobalt-containing hydroxide dodecyl sulphates are easily oxidized to mixed LDH/LHS phases. The subsequent anion exchange, delamination and nanosheets restacking lead to the full transformation into the pure LDH phase.

5) Anion exchange affords layered hydroxides with higher delamination capability in the comparison with the hydroxides prepared by direct precipitation. The delamination is facilitated by high phase-purity and by using dodecyl sulphate precursors.

6) Prepared colloid dispersions contain single nanometric hydroxide sheets and are stable without aggregation in long time-scale of several months. The colloids can be prepared in a wide range of concentrations up to 30 $mg \cdot mL^{-1}$, more concentrated dispersion forms gels composed of aggregated nanosheets.

7) Diluted colloids can be used successfully for the preparation of oriented films by conventional methods such as drop casting, spin coating, or layer-by-layer method. The AFM images of spin coated films shows nanometric nanosheets with the flat surface, documenting that spin coating is the most suitable method for the ultrathin film preparation.

8) Hydroxide nanosheets can be utilized for the ultrathin electrode fabrication. Nickel hydroxide nanosheets show typical $Ni(OH)_2$ electrochemical behaviour with some structural rearrangement due to counter ion incorporation without the loss of electrochemical efficiency.

9) Cobalt hydroxide nanosheets show typical $Co(OH)_2$ electrochemical behaviour without structural changes. Thanks to the ultrathin thickness, these electrodes have very fast electrochemical response at high scan rates due to the suppression of counter ion diffusion.

10) Voltammetric study of nickel-cobalt hydroxide nanosheets indicates that Co-doping effectively improves the performance of the nanosheets by decreasing the time of their electrochemical activation, which for the pure nickel hydroxide nanosheets requires much more potential sweeps. The observed electrochemical response can be ascribed to mutual compensation of the cobalt and nickel response *via* electron sharing between these metals in the hydroxide nanosheets. Evidently, mutual interactions of both metal centres in the nanosheets are much stronger than in the bulk layered material. This effect may have significance for the utilization of metal hydroxide nanosheets in capacitors and other charge storage devices.

5. References

1 N.N. Greenwood, A. Earnshaw, Chemie prvků, Informatorium, Praha 1993.

2 V. Nicolosi, M. Chhowalla, M. G. Kanatzidis, M. S. Strano, J. N. Coleman, Science, 2013, 340, 1226419.

3 R. Mas-Ballest, C. Gomez-Navarro, J. Gomez-Herrero, F. Zamora, Nanoscale, 2011, 3, 20-30.

4 S. Niyogi, E. Bekyarova, M. E. Itkis, J. L. McWilliams, M. A. Hamon, R. C. Haddon, *J. Am. Chem. Soc*., **2006**, *128*, 7720-7721.

5 D. D. L. Chung, *J. Mater. Sci*., **2002**, *37*, 1475-1489.

6 M. Zanetti, S. Lomakina, G. Camino, *Macromol. Mater. Eng*., **2000**, *279*, 1-9.

7 M. Chhowalla, H. S. Shin, G. Eda, L. J. Li, K. P. Loh, H. Zhang , *Nature Chemistry*, **2013**, *5*, 263-275.

8 C. C. Coleman, H. Goldwhite, W. Tikkanen, *Chem. Mater*., **1998**, *10*, 2794-2800.

9 M. Osada, T. Sasaki, *J. Mater. Chem*., **2009**, *19*, 2503–2511.

10 H. B. Wu, J. S. Chen, H. H. Hng, X. W. Lou, *Nanoscale*, **2012**, *4*, 2526-2542.

11 X. Han, Q. Kuang, M. Jin, Z. Xie, L. Zheng, *J. Am. Chem. Soc*., **2009**, *131*, 3152-3153.

12 D. G. Evans, X. Duan, *Chem. Commun*., **2006**, 485-496.

13 G. G. C. Arizaga, K. G. Satyanarayana, F. Wypych, *Solid State Ionics*, **2007**, *178*, 1143-1162.

14 W. J. Roth, P. Nachtigall, R. E. Morris, *J. Čejka, Chem.Rev*., **2014**, *114*, 4807–4837.

15 A. Lerf, *Dalton Trans*., **2014**, *43*, 10276-10291.

16 U. Díaz, A, Corma, *Dalton Trans*., **2014**, *43*, 10292–10316.

17 J. L. C. Rowsell, O. M. Yaghi, *Micropor. Mesopor. Mat*., **2004**, *73*, 3-14.

18 V. R. L. Constantino, C. A. S. Barbosa, M. A. Bizeto, P. M. Dias, *An. Acad. Bras. Ci*., **2000**, *72*, 45-49.

19 N. Emery, C. Herold, P. Lagrange, *Prog. Solid State Ch*., **2008**, *36*, 213-222.

20 S. Flandrois , B. Simon, *Carbon*, **1999**, *37*, 165-180.

21 M. Winter, R. J. Brodd, *Chem. Rev*. **2004**, *104*, 4245-4269.

22 T. Selvam, A. Inayat, W. Schwieger, *DaltonTrans*., **2014**,.*43*, 10365-10387.

23 S. Pavlidou, C. D. Papaspyrides, *Prog. Polym. Sci*., **2008**, *33*, 1119-1198.

24 M. Xu, T. Liang, M. Shi, H. Chen, *Chem. Rev*., **2013**, *113*, 3766-3798.

25 K. S. Novoselov, *Rev. Mod. Phys.*, **2011**, *83*, 837-849.

26 A. Geim, *Angew. Chem*., **2011**, *50*, 6967-6985.

27 R. Ma, T. Sasaki, *Adv. Mater*., **2010**, *22*, 5082-5104.

28 Y. Hu, H. Qian, T. Mei, J. Guo, T. White, *Mater. Lett*., **2010**, *64*, 1095-1098.

29 T. Shibata, G. Takanashi, T. Nakamura, K. Fukuda, Y. Ebina, T. Sasaki, *Energy Environ. Sci*., **2011**, *4*, 535-542.

30 X. Huang, Z. Zeng, H. Zhang, *Chem. Soc. Rev*., **2013**, *42*, 1934-1946.

31 Y. Lin, J. W. Connell, *Nanoscale*, **2012**, *4*, 6908-6939.

32 Ch. W. Chiu, T. K. Huang, Y. Ch. Wang, B. G. Alamani, J. J. Lin, *Prog. Polym. Sci*., **2014**, *39*, 443-485.

33 Q. Wang, D. O'Hare, *Chem. Rev*., **2012**, *112*, 4124-4155.

34 N. Miyamoto, T. Nakato. *Isr. J. Chem*., **2012**, *52*, 881-894.

35 Y. Yao, Z. Li, Z. Lin, K. S. Moon, J. Agar, C. Wong, *J. Phys. Chem. C*, **2011**, *115*, 5232-5238.

36 G. Rogez, C. Massobrio, P. Rabu, M. Drillon, *Chem. Soc. Rev*., **2011**, *40*, 1031-1058.

37 X. Guo, F. Zhang, D. G. Evans, X. Duan, *Chem. Commun*., **2010**, *46*, 5197-5210.

38 N. Iyi, Y. Ebina, T. Sasaki, *Langmuir*, **2008**, *24*, 5591-5598.

39 Z. Liu, R. Ma, M. Osada, N. Iyi, Y. Ebina, K. Takada, T. Sasaki, *J. Am. Chem. Soc*., **2006**, *128*, 4872-4880.

40 J. Hynek, V. Kalousek, R. Zouzelka, P. Bezdicka, P. Dzik, J. Rathousky, J. Demel, K. Lang, *Langmuir*, **2014**, *30*, 380-386.

41 G. Decher, M. Eckle, J. Schmitt, B. Struth, *J. Coll. Int. Sci*., **1998**, *3*, 32-39.

42 D. Yan, J. Lu, M. Wei, S. Qin, L. Chen, S. Zhang, D. G. Evans, X. Duan, *Adv. Funct. Mater*., **2011**, *21*, 2497-2505.

43 W. Shi, Y. Lin, X. Kong, S. Zhang, Y. Jia, M. Wei, D. G. Evans, X. Duan, *J. Mater. Chem*., **2011**, *21*, 6088-6094.

44 K. Holmberg, *J. Coll. Int. Sci*., **2004**, *274*, 355-364.

45 A. Wongariyakawee, F. Schaeffel, J. H. Warner, D. O'Hare, *J. Mater. Chem*., **2012**, *22*, 7751-7756.

46 G.D. Yuan, W.J. Zhang, Y. Yang, Y.B. Tang, Y.Q. Li, J.X. Wang, X.M. Meng, Z.B. He, C.M.L. Wu, I. Bello, C.S. Lee, S.T. Lee, *Chemical Physics Letters*, **2009**, *467*, 361-364.

47 K. S. Novoselov, D. Jiang, F. Schedin, T. J. Booth, V. V. Khotkevich, S. V. Morozov, and A. K. Geim, *PNAS*, **2005**, *102*, 10451-10453.

48 S. Park, R. S. Ruoff, *Nat. Nanotechnol*. **2009**, *4*, 217-224.

49 D. R. Dreyer, S. Park, Ch. W. Bielawski, R. S. Ruoff, *Chem. Soc. Rev*., **2010**, *39*, 228-240.

50 J. T. Han, J. I. Jang, H. Kim, J. Y. Hwang, H. K. Yoo, J. S. Woo, S. Choi, H. Y. Kim, H. J. Jeong, S. Y. Jeong, K. J. Baeg, K. Cho, G. W. Lee, *Scientific Reports*, **2014**, *4*, 5133.

51 X. Duan, D. G. Evans, *Layered Double Hydroxides*, Springer-Verlag, Berlin, **2006**, vol. 119,

52 A. I. Khan, D. O'Hare, *J. Mater. Chem.*, **2002**, *12*, 3191-3198.

53 G. Rogez, C. Massobrio, P. Rabu, M. Drillon, *Chem. Soc. Rev.*, **2011**, *40*, 1031-1058.

54 T. Hibino, M. Kobayashi, *J. Mater. Chem*., **2005**, *15*, 653–656.

55 C. Nethravathi, B. Viswanath, M. Sebastian, M. Rajamathi, *J. Colloid Interface Sci.*, **2010**, *345*, 109–115.

56 N. Mao, C. H. Zhou, D. S. Tonga, W. H. Yua, C. X. C. Lin, *Applied Clay Science*, **2017**, 144, 60–78.

57 S. P. Newman, W. Jones, *J. Solid State Chem.*, **1999**, *148*, 26-40.

58 J. Demel, J. Hynek, P. Kovář, Y. Dai, C. Taviot-Guého, O. Demel, M. Pospíšil, K. Lang, *J. Phys. Chem. C*, **2014**, *118*, 27131-2714.

59 J. Liang, R. Ma, T. Sasaki, *Dalton Trans.*, **2014**, *43*, 10355-10364.

60 E. L. Crepaldi, P. C. Pavan, J. B. Valim, *Chem. Commun.*, **1999**, 155-156.

61 V. Gupta, T. Kusahara, H. Toyama S. Gupta, N. Miura, *Electrochem. Commun.*, **2007**, *9*, 2315-2319.

62 R. Ma, K. Takada, K. Fukuda, N. Iyi, Y. Bando, T. Sasaki, *Angew. Chem. Int. Ed.*, **2008**, *47*, 86-89.

63 M. Taibi, S. Ammar, N. Jouini, F. Fiévet, P. Molinié, M. Drillon, *J. Mater. Chem.*, **2002**, *12*, 3238-3244.

64 K. Nakamoto, *Infrared and Raman Spectra of Inorganic and Coordination Compounds*, Wiley, New York, 4th edn, **1986**, pp. 231-233.

65 R. Ma, Z. Liu, K. Takada, K. Fukuda, Y. Ebina, Y. Bando, T. Sasaki, *Inorg. Chem*. **2006**, *45*, 3964-3969.

66 J. Demel, K. Lang, *Eur. J. Inorg. Chem.* **2012**, 5154-5164.

67 W. Shi, Y. Lin, X. Kong, S. Zhang, Y. Jia, M. Wei, D. G. Evans, X. Duan, *J. Mater. Chem.*, **2011**, *21*, 6088-6094.

68 N. Chu, Y. Sun, Y. Zhao, X. Li, G. Sun, S. Ma, X. Yang, Dalton Trans., **2012**, *41*, 7409-7414.

69 M. X. Reinholdt, R. J. Kirkpatrick, *Chem. Mater*. **2006**, *18*, 2567-2576.

70 A. Vyalikh, F. R. Costa, U. Wagenknecht, G. Heinrich, D. Massiot, U. Scheler, J. Phys. Chem. C, **2009**, *113*, 21308–21313.

71 M. Sipiczki, E. Kuzmann, I. Pálinkó, Z. Homonnay, P. Sipos, Á. Kukovecz, Z. Kónya, Hyperfine Interact., **2013**, *217*, 145-149.

72 N. S. Puttaswamy, P. Vishnu Kamath, *J. Mater. Chem*., **1997**, *7*, 1941-1945.

73 J. Demel, J. Pleštil, P. Bezdička, P. Janda, M. Klementová, K. Lang, *J. Colloid Interface Sci*., **2011**, *360*, 532–539.

74 C. D. Putnam, M. Hammel, G. L. Hura, J. A. Tainer, *Q. Rev. Biophys*., **2007**, *40*, 191-285.

75 F. Kovanda, D. Koloušek, R. Kalousková, Z. Vymazal, *Chem. Listy*, **2001**, *95*, 493-497.

76 F. Leroux, J. P. Besse, *Chem. Mater*. **2001**, *13*, 3507-3515.

77 L. A. Utracki, M. Sepehr, E. Boccaleri, *Polym. Adv. Technol*. **2007**, 18, 1-37.

78 Y. Lin, J. Wang, D. G. Evans, D. Li, *J. Phys. Chem. Solids*, **2006**, *67*, 998-1001.

79 Y. Gao, J. Wu, Q. Wang, C. A. Wilkie, D. O'Hare, *J. Mater. Chem. A*, **2014**, *2*, 10996-11016.

80 Z. Matusinovic, C, A. Wilkie, *J. Mater. Chem*., **2012**, *22*, 18701-18704.

81 G. Fan, F. Li, D. G. Evans, X. Duan, *Chem. Soc. Rev*., **2014**, *43*, 7040-7066.

82 Z. P. Xu, J. Zhang, M. O. Adebajo, H. Zhang, C. Zhou, *Appl. Clay Sci.*, **2011**, *53*, 139-150.

83 C. Li, M. Wei, D. G. Evans, X. Duan, *Catalysis Today*, **2015**, 247, 163–169.

84 C. Qiao, Y. Zhang, Y. Zhu, C. Cao, X. B. J. Xu, *J. Mater. Chem. A*, **2015**, *3*, 6878-6883.

85 Zhang, J. Zhao, L. Zhou, Z. Li, M. Shao, M Wei, *J. Mater. Chem. A*, **2016**, *4*, 11516-11523.

86 J. Hynek, V. Kalousek, R. Zouzelka, P. Bezdicka, P. Dzik, J. Rathousky, J. Demel, K. Lang, *Langmuir*, **2014**, *30*, 380-386.

87 K. H. Goh, T. T. Lim, Z. Dong, *Water Res*., **2008**, *42*, 1343-1368.

88 J. H. Choy, S. J. Choi, J. M. Oh, T. Park, *Appl. Clay Sci.*, **2007**, *36*, 122-132.

89 N. B. Allou, P. Saikia, A. Borah, R. L. Goswamee, *Colloid Polym Sci.*, **2017**, *295*, 725–747.

90 K. Zhang, Z. P. Xu, J. Lu, Z. Y. Tang, H. J. Zhao, D. A. Good, M. Q. Wei, *Int. J. Mol. Sci*. **2014**, *15*, 7409-7428.

91 A. Li, L. Qin, W. Wang, R. Zhu, Y. Yu, H. Liu, S. Wang, *Biomaterials*, **2011**, *32*, 469-477.

92 D. Hesse, M. Badar, A. Bleich, A. Smoczek, S. Glage, M. Kieke, P. Behrens, P. P. Muller, K. H. Esser, M. J. Stieve, *Mater. Sci. Mater. Med*., **2013**, *24*, 129-136.

93 J. P. Cheng, J. Zhang, F. Liu, *RSC Adv*., **2014**, *4*, 38893-38917.

94 G. Wang, L. Zhang, J. Zhang, *Chem. Soc. Rev*., **2012**, *41*, 797-828.

95 P. Vialat, F. Leroux, C Mousty, *J. Solid State Electrochem*., **2015**, *19*, 1975-1983

96 A. Harvey, X. He, I. J. Godwin, C. Backes, D. McAteer, N. C. Berner, N. McEvoy, A. Ferguson, A. Shmeliov, M. E. G. Lyons, V. Nicolosi, G. S. Duesberg, J. F. Doneganab, J. N. Coleman, *J. Mater. Chem. A*, **2016**, 4, 11046–11059.

97 X. Li, D. Du, Y. Zhang, W. Xing, Q. Xue, Z. Yan, *J. Mater. Chem. A*, **2017**, 5, 15460–15485.

98 J. Zhao, J. Chen, S. Xu, M. Shao, D. Yan, M. Wei, D. G. Evans, X. Duan, *J. Mater. Chem. A*, **2013**, *1*, 8836-8843.

99 A. Mignani, E. Scavetta, D. Tonelli, *Anal. Chim. Acta*, **2006**, *577*, 98-106.

100 M. Li, J. E. Zhu, L. Zhang, X. Chen, H. Zhang, F. Zhang, S. Xu, D. G. Evans, *Nanoscale*, **2011**, *3*, 4240-4246.

101 P. Lu, Y. Lei, S. Lu, Q. Wang, Q. Liu, *Anal. Chim. Acta*, **2015**, *880*, 42–51.

102 M. Rajamathi, P. V. Kamath, R. Seshadrib, *J. Mater. Chem*., **2000**, *10*, 503-506.

103 Z. P. Xu, H. C. Zeng, *Chem. Mater*., **1999**, *11*, 67-74.

104 L. Poul, N. Jouini, F. Fiévet, *Chem. Mater*., **2000**, *12*, 3123-3132.

105 L. Wang, C. Lin, F. Zhang, Jian Jin, *ACS Nano*, **2014**, *8*, 3724-3734.

106 J. M. Ko, D. Soundarajan, J. H. Park, S. D. Yang, S. W. Kim, K. M. Kim and K. H. *Yu, Curr. Appl. Phys*., **2012**, *12*, 341–345.

107 V. Gupta, S. Gupta, N. Miura, *J. Power Sources*, **2008**, *175*, 680-685.

108 W. K. Hu, D. Noréus, *Chem. Mater*., **2003**, *15*, 974-978.

109 C. Nethravathi, N. Ravishankar, C. Shivakumara, M. Rajamathi, *J. Power Sources*, **2007**, *172*, 970-974.

110 A. Delahaye-Vidal, B. Beaudoin, N. Sac-Epée, K. Tekaia-Elhsissen, A. Audemer, M. Figlarz, *Solid State Ionics*, **1996**, *84*, 239-248.

111 J. W. Lee, T. Ahn, D. Soundararajan, J. M. Koc, J. D. Kim, *Chem. Commun*., **2011**, *47*, 6305-6307.

112 H. Wang, H. S. Casalongue, Y. Liang, H. Dai, *J. Am. Chem. Soc*., **2010**, *132*, 7472-7477.

113 H. Wang, X. Xiang, F. Li, *J. Mater. Chem*., **2010**, *20*, 3944-3952.

114 X. Bai, Q. Liu, H. Zhang, J. Liu, Z. Li, X. Jing, Y. Yuan, L. Liu, J. Wang, *Electrochim. Acta*, **2016**, *215*, 492–499.

115 X. Liu, R. Ma, Y. Bando, T. Sasaki, *Adv. Mater*., **2012**, *24*, 2148-2153.

116 C. Yuan, X. Zhang, B. Gao, J. Li, *Mater. Chem. Phys*., **2007**, 101, 148-152.

117 G. Nagaraju, G. S. R. Raju, Y. H. Ko, J. S. Yu, *Nanoscale*, **2016**, 8, 812–825.

118 N. Arencibia, V. Oestreicher, F. A. Viva, M. Jobbágy, *RSC Adv*., **2017**, 7, 5595–5600.

119 Z. Lv, Q. Zhong, Y. Bu, *Electrochimica Acta*, **2016**, *215*, 500–505.

120 B. Schneiderová, J. Demel, J. Pleštil, P. Janda, J. Bohuslav, D. Ihiawakrim, O. Ersen, G. Rogez, K. Lang, *J. Mater. Chem. A*, **2013**, *1*, 11429–11437.

121 B. Schneiderová, J. Demel, J. Pleštil, H. Tarábková, J. Bohuslav, K. Lang, *Dalton Trans*., **2014**, *43*, 10484–10491.

122 B. Schneiderová, J. Demel, A. Zhigunov, J. Bohuslav, H. Tarábková, P. Janda, K. Lang, *J. Colloid Interface Sci*., **2017**, *499*, 138–144.